Research Square

Preprints are preliminary reports that have not undergone peer review.
They should not be considered conclusive, used to inform clinical practice,
or referenced by the media as validated information.

An injectable chitosan depot co-delivering elemental Mo^0 and α-MnO_2 suppresses the growth of established clear cell renal cell carcinoma after a single intratumoral injection

Tingting Sun
The Affiliated Huaian No.1 People's Hospital of Nanjing Medical University
Xuzhong Liu
The Affiliated Huaian No.1 People's Hospital of Nanjing Medical University
Zeping Gui
Jiangsu Key Laboratory of Urological Disease Prevention and Treatment, The Second Affiliated Hospital of Nanjing Medical University, Nanjing Medical University
Jian Hu
The Affiliated Huaian No.1 People's Hospital of Nanjing Medical University
Peng Lu
lupeng324@njmu.edu.cn

The Affiliated Huaian No.1 People's Hospital of Nanjing Medical University

Research Article

Keywords: clear cell renal cell carcinoma, intratumoral drug delivery, injectable thermoresponsive hydrogel, ferroptosis, manganese dioxide, elemental molybdenum

Posted Date: November 18th, 2026

DOI: https://doi.org/10.21203/rs.3.rs-11412062/v1

License: This work is licensed under a Creative Commons Attribution 4.0 International License.
Read Full License

Additional Declarations: No competing interests reported.

An injectable chitosan depot co-delivering elemental Mo^0 and α-MnO_2 suppresses the growth of established clear cell renal cell carcinoma after a single intratumoral injection

Tingting Sun[1]; Xuzhong Liu[2]; Zeping Gui[3]; Jian Hu[1]* and Peng Lu[4]*

1. Department of Pediatrics, The Affiliated Huai'an No. 1 People's Hospital of Nanjing Medical University, Huai'an 223300, China
2. Department of Urology, The Affiliated Huai'an No. 1 People's Hospital of Nanjing Medical University, Huai'an 223300, China
3. Department of Urology, Jiangsu Key Laboratory of Urological Disease Prevention and Treatment, The Second Affiliated Hospital of Nanjing Medical University, Nanjing Medical University, Nanjing 210011, China.
4. Department of Geriatrics, The Affiliated Huai'an No. 1 People's Hospital of Nanjing Medical University, Huai'an 223300, China.

* Correspondence: 13852398989@163.com; lupeng324@njmu.edu.cn

Abstract

Background/Objectives: Local control remains difficult for patients with locally advanced or unresectable clear cell renal cell carcinoma (ccRCC) who are unsuitable for surgery or systemic therapy. We developed an injectable, thermoresponsive chitosan/β-glycerophosphate hydrogel co-loaded with elemental molybdenum (Mo^0) and α-phase manganese dioxide (α-MnO_2) as a locally retained intratumoral depot. **Methods:** Physicochemical properties, redox activity, and Mo/Mn release in phosphate-buffered saline with or without 0.2 mM H_2O_2 were characterized. Cytotoxicity and ferroptosis-associated responses were evaluated in 786-O and A498 ccRCC cells and HK-2 renal tubular epithelial cells using biochemical, molecular, and pharmacological-rescue assays. Antitumor efficacy, tolerability, and elemental biodistribution were assessed after a single 50 μL intratumoral injection in mice bearing established subcutaneous 786-O tumors. **Results:** CS+MoMn formed a porous, predominantly elastic, self-recovering gel and produced higher Mo and Mn concentrations in the release medium under oxidative conditions during the 14-day study. CS+MoMn reduced A498 and 786-O viability to approximately 35% and 30% respectively, whereas HK-2 viability remained approximately 92%. Treatment depleted glutathione; increased C11-BODIPY oxidation, malondialdehyde, labile Fe^{2+}, and 4-hydroxynonenal; suppressed SLC7A11 and GPX4; and increased TFRC and ACSL4.

Ferrostatin-1, liproxstatin-1, and deferoxamine substantially rescued tumor-cell viability, and key responses were reproduced in A498 cells. In vivo, CS+MoMn reduced final tumor volume from approximately 580 to 65 mm^3 and tumor weight from 0.75 to 0.06 g relative to the blank hydrogel. No overt short-term histopathological, hematological, or biochemical abnormalities were detected, although limited distal elemental distribution occurred. **Conclusions:** The Mo^0/α-MnO_2-loaded hydrogel provides a locally retained, oxidation-responsive platform that preferentially induces ferroptosis-associated ccRCC cell death in vitro and suppresses established tumor growth after a single intratumoral administration.

Keywords: clear cell renal cell carcinoma; intratumoral drug delivery; injectable thermoresponsive hydrogel; ferroptosis; manganese dioxide; elemental molybdenum

1. Introduction

Renal cell carcinoma (RCC) is a common urological malignancy, and clear cell renal cell carcinoma (ccRCC) accounts for most RCC cases [1,2]. Approximately one in five patients presents with locally advanced or metastatic disease, and a similar proportion of patients treated for apparently localized tumors subsequently experience recurrence [3]. For patients with unresectable primary tumors or those who are unsuitable for surgery because of severe comorbidities, a solitary kidney, or impaired renal function, systemic therapy remains the principal treatment option [3]. Current first-line regimens combine immune-checkpoint blockade with a vascular endothelial growth factor receptor tyrosine kinase inhibitor or employ dual immune-checkpoint inhibition [4–6]. Although these regimens have substantially improved survival, objective responses were achieved in only 42–59% of patients in pivotal clinical trials [4–6], indicating that a considerable proportion of patients obtain no meaningful tumor shrinkage. Moreover, systemic treatment generally requires continuous exposure and is associated with cumulative toxicity. In the registration trial of sunitinib, 32% of patients required dose reduction, and 8% discontinued treatment because of adverse events [7]. Similarly, despite using planned treatment interruptions, the STAR trial reported grade 3 or higher hypertension in approximately one-quarter of participants [8]. Consequently, patients who progress after available systemic therapies or cannot tolerate them may have limited options for controlling a defined and accessible tumor mass. Local therapy addresses a distinct clinical need. When a dominant tumor

lesion is anatomically defined and accessible by needle, direct intratumoral administration can generate high local therapeutic concentrations that would be difficult to achieve through systemic delivery, while reducing the total administered dose and systemic exposure [9,10]. Intratumoral delivery may also partly overcome limitations associated with systemic drug distribution within solid tumors. Vessel spacing, elevated interstitial pressure, and dense extracellular matrix can produce highly heterogeneous drug penetration, leaving tumor cells located far from functional blood vessels exposed to substantially lower drug concentrations than those measured in plasma [11].

Injectable thermosensitive hydrogels provide a practical platform for localized intratumoral delivery. Chitosan/β-glycerophosphate systems remain fluid at low temperatures, undergo gelation near physiological temperature, adhere to tissues, and have an established record of biocompatibility [12]. Unlike freely injected drug solutions, which may disperse along the needle tract or leak into surrounding tissues, an in situ-forming hydrogel can retain its therapeutic cargo at the injection site and provide sustained local release. These properties have supported the development of hydrogel depots for image-guided intratumoral drug delivery [13]. However, local retention alone is insufficient; the therapeutic cargo must exploit a biologically relevant vulnerability of ccRCC. Clear cell renal carcinoma cells accumulate lipids and glycogen, and their enrichment in polyunsaturated lipid species increases their dependence on glutathione peroxidase 4 (GPX4) to prevent phospholipid peroxidation [14–17]. Upstream of GPX4, the cystine/glutamate antiporter SLC7A11 supports intracellular glutathione synthesis by supplying cystine for cysteine production [18]. These metabolic features create a potential susceptibility to ferroptosis, an iron-dependent form of regulated cell death driven by uncontrolled lipid peroxidation [19,20]. Disrupting the glutathione-dependent antioxidant system may therefore push ccRCC cells beyond their capacity to control lipid-peroxidative damage.

Based on this rationale, we designed a dual-particle system combining α-phase manganese dioxide (α-MnO_2) and elemental molybdenum (Mo^0). α-MnO_2 reacts with glutathione, producing glutathione disulfide and Mn^{2+} and thereby depleting the intracellular reducing pool; it can also catalytically decompose H_2O_2 [21–24]. Mo^0 was incorporated to provide a sustained local oxidative stimulus. Elemental molybdenum was selected instead of the molybdate salts and molybdenum sulfides more commonly investigated in nanomedicine because the

physicochemical and biological properties reported for these chemically distinct molybdenum species cannot be directly extrapolated to Mo^0. Accordingly, we developed an injectable chitosan/β-glycerophosphate hydrogel co-loaded with α-MnO_2 and Mo^0 as a locally retained, redox-responsive therapeutic depot. We characterized the particles and composite hydrogel, evaluated their redox-responsive elemental release, and compared their cytotoxic effects in ccRCC cells and normal renal tubular epithelial cells. We then investigated the contribution of ferroptosis using biochemical, molecular, and pharmacological-rescue analyses. Finally, we examined whether a single intratumoral administration could suppress the growth of established tumors while evaluating systemic tolerability and elemental biodistribution. This study therefore tests whether localized disruption of glutathione-dependent redox defense can provide selective and sustained control of ccRCC.

2. Materials and methods

2.1 Reagents

Chitosan (medium molecular weight, 190–310 kDa, 75–85% deacetylated; Sigma-Aldrich, 448877) and β-glycerophosphate disodium salt hydrate (Sigma-Aldrich, G9422) formed the hydrogel matrix, the latter used as a single fixed lot throughout. Molybdenum nanopowder (Mo; nominal particle size, 35–45 nm; 99.9% purity, metal basis; US Research Nanomaterials, Inc., US1112) and α-MnO_2 nanopowder (nominal particle size, 100 nm; ATOMFAIR LLC, AF-FM-C-MNO2-100A-SP00) were used as received. Hydrochloric acid (Sigma-Aldrich, 320331), hydrogen peroxide 30% (Sigma-Aldrich, H1009) and phosphate-buffered saline (Thermo Fisher Scientific, 10010023) were of analytical grade.

Cell culture media included RPMI-1640 (Thermo Fisher Scientific, 11875093), Minimum Essential Medium (MEM; Thermo Fisher Scientific, 11095080), and DMEM/F-12 (Thermo Fisher Scientific, 11330032), fetal bovine serum (Thermo Fisher Scientific, 10099141), penicillin–streptomycin (Thermo Fisher Scientific, 15140122) and 0.25% trypsin-EDTA (Thermo Fisher Scientific, 25200056).

Pharmacological agents were ferrostatin-1 (Sigma-Aldrich, SML0583), liproxstatin-1 (Sigma-Aldrich, SML1414), Z-VAD-FMK (Selleck Chemicals, S7023), deferoxamine mesylate (DFO; Selleck Chemicals, S5742), and mitomycin C (Sigma-Aldrich, M4287), each reconstituted per supplier instructions and stored as single-use aliquots at −80 °C.

Assays used Cell Counting Kit-8 (Dojindo, CK04), propidium iodide (Sigma-Aldrich, P4170), C11-BODIPY 581/591 (Thermo Fisher Scientific, D3861), 2′,7′-dichlorofluorescin diacetate (Beyotime, S0033), the Lipid Peroxidation MDA Assay Kit (Beyotime, S0131), the GSH and GSSG Assay Kit (Beyotime, S0053), FerroOrange (Dojindo, F374), the Annexin V-FITC/PI Apoptosis Detection Kit (Beyotime, C1062), Alexa Fluor 488 phalloidin (Thermo Fisher Scientific, A12379), DAPI (Sigma-Aldrich, D9542), crystal violet (Sigma-Aldrich, C0775), the In Situ Cell Death Detection Kit TMR red (Roche, 12156792910) and haematoxylin and eosin (Sigma-Aldrich, HHS32 and HT110232). Transwell inserts of 8 μm pore size (Corning, 3422) were used for migration assays and 24-well plates (Corning, 3524) throughout.

Primary antibodies used for Western blotting were anti-GPX4 (Abcam, ab125066), anti-SLC7A11 (Cell Signaling Technology, 12691), anti-ACSL4 (Abcam, ab155282), anti-TFRC (Cell Signaling Technology, 13113), anti-FTH (Abcam, ab75972), anti-4-hydroxynonenal (4-HNE; Abcam, ab46545), anti-NRF2 (Cell Signaling Technology, 12721), anti-HO-1 (Cell Signaling Technology, 43966), anti-caspase-3 (Proteintech, 19677-1-AP), anti-cleaved PARP1 (Abcam, ab32064), anti-BAX (Cell Signaling Technology, 5023), and anti-BCL-2 (Cell Signaling Technology, 4223). Anti-Ki-67 (Abcam, ab15580) was used for immunohistochemistry. Loading-control antibodies were anti-α-tubulin (Cell Signaling Technology, 3873), anti-β-actin (Cell Signaling Technology, 4970), and anti-GAPDH (Cell Signaling Technology, 5174). Secondary antibodies for Western blotting were horseradish peroxidase (HRP)-conjugated goat anti-rabbit IgG (Cell Signaling Technology, 7074) and HRP-conjugated horse anti-mouse IgG (Cell Signaling Technology, 7076). For dual immunofluorescence staining, rabbit anti-SLC7A11 (Proteintech, 26864-1-AP) and mouse anti-GPX4 (Proteintech, 67763-1-Ig) were used as primary antibodies. SLC7A11 and GPX4 were visualized using Alexa Fluor 594-conjugated goat anti-rabbit IgG (Thermo Fisher Scientific, A-11037) and Alexa Fluor 488-conjugated goat anti-mouse IgG (Thermo Fisher Scientific, A-11029), respectively.

Reverse transcription and quantitative PCR used the PrimeScript RT Reagent Kit with gDNA Eraser (Takara, RR047A) and TB Green Premix Ex Taq II (Takara, RR820A). Water throughout was sterile and pyrogen-free. Reduced L-glutathione (GSH; Sigma-Aldrich, G4251) and 5,5′-dithiobis(2-nitrobenzoic acid) (DTNB; Sigma-Aldrich, D8130) were used for the cell-

free GSH depletion assay. The Amplex Red Hydrogen Peroxide/Peroxidase Assay Kit (Invitrogen, Thermo Fisher Scientific, A22188) was used to quantify residual H_2O_2 in the cell-free assay.

2.2 Instrumentation

Particle morphology was examined on a JEM-1400 transmission electron microscope (JEOL) and hydrogel microstructure on an SU8010 field-emission scanning electron microscope (Hitachi). Hydrodynamic size and ζ-potential were measured on a Zetasizer Nano ZS (Malvern Panalytical), surface composition on a K-Alpha X-ray photoelectron spectrometer (Thermo Fisher Scientific), crystalline phase on a D8 Advance diffractometer (Bruker) and infrared spectra on a Nicolet iS50 FTIR spectrometer (Thermo Fisher Scientific). Rheology was performed on an MCR 302 rheometer (Anton Paar) and injection force on a TA.XTplus texture analyser (Stable Micro Systems). Elemental quantification used an Agilent 7900 ICP-MS. Absorbance and fluorescence were read on a Synergy H1 plate reader (BioTek), flow cytometry on a FACSCanto II (BD Biosciences), and fluorescence imaging on an LSM 900 confocal microscope (Zeiss). Chemiluminescent membranes were imaged on a ChemiDoc MP system (Bio-Rad) and quantified in Image Lab, and quantitative PCR was run on a CFX96 Touch thermocycler (Bio-Rad). Haematology and serum chemistry were analysed on a BC-5000 Vet analyser (Mindray) and a Chemray 240 (Rayto). Elemental mapping was performed using an energy-dispersive X-ray spectroscopy (EDS) system coupled to the JEM-1400 transmission electron microscope (JEOL, Japan). Hydrogel samples were lyophilised using a FreeZone 2.5 L freeze-dryer (Labconco, USA). Samples for ICP–MS analysis were subjected to microwave-assisted acid digestion using a MARS 6 microwave digestion system (CEM Corporation, USA).

2.3 Preparation of CS/β-GP Hydrogels Co-Loaded with Mo^0 and α-MnO2

CS/β-GP hydrogels were prepared using a modified thermosensitive chitosan/polyol-salt approach described by Chenite and colleagues [12]. Commercial Mo^0 and α-MnO_2 nanoparticles were separately dispersed in sterile water at 2 mg/mL and sonicated for 5 min in an ice-water bath immediately before use. Chitosan was dissolved in 0.1 mol/L HCl to prepare a 2.0% (w/v) stock solution and stirred at 4 °C until completely dissolved. A 50% (w/v) β-glycerophosphate sodium (β-GP) stock solution was separately prepared in sterile water and pre-cooled to 4 °C. For each 1 mL batch of the co-loaded formulation, 12.5 µL of the Mo^0 dispersion and 62.5 µL of the α-MnO_2 dispersion were mixed, corresponding to a Mo^0:α-MnO_2 particle mass ratio of 1:5.

The mixed dispersion was added to 750 μL of the chitosan stock solution under continuous stirring in an ice bath, followed by the slow dropwise addition of 160 μL of the pre-cooled β-GP stock solution. The pH was measured and, when necessary, adjusted to 7.0–7.4 using small volumes of NaOH or HCl solution. Sterile water was added to obtain a final volume of 1 mL, including the volume used for pH adjustment. The nominal final concentrations of chitosan and β-GP were 1.5% and 8.0% (w/v), respectively, and those of Mo^0 and α-MnO_2 particles were 0.025 and 0.125 mg/mL, respectively.

Four CS/β-GP hydrogel formulations were prepared: a nanoparticle-free hydrogel (Control), an α-MnO_2-loaded hydrogel (CS+Mn), a Mo^0-loaded hydrogel (CS+Mo), and an α-MnO_2/Mo^0 co-loaded hydrogel (CS+MoMn). Each formulation contained 750 μL of the chitosan stock solution and 160 μL of the β-GP stock solution. CS+Mn and CS+Mo were supplemented with 62.5 μL of the α-MnO_2 dispersion and 12.5 μL of the Mo^0 dispersion, respectively, whereas CS+MoMn contained both dispersions at the same respective volumes. No nanoparticles were added to the Control formulation. The pH of each formulation was adjusted to 7.0–7.4, and the final volume was brought to 1 mL with sterile water, maintaining identical nominal chitosan and β-GP concentrations across groups. The precursor formulations were maintained at 4 °C and subsequently incubated at 37 °C to induce thermal gelation before further experiments.

2.4 Physicochemical characterisation

The morphology and aggregation of α-MnO_2, Mo^0, and the mixed α-MnO_2/Mo^0 samples were examined by transmission electron microscopy, and their elemental composition and spatial distribution were analysed by energy-dispersive X-ray spectroscopy. The surface elemental composition and chemical states of the mixed sample were investigated by X-ray photoelectron spectroscopy, including the survey spectrum and high-resolution O 1s, Mn 2p, and C 1s spectra. The chemical bonds and surface functional groups were analysed by Fourier-transform infrared spectroscopy over a wavenumber range of 4000–400 cm^{-1}. The hydrodynamic particle-size distributions of the different dispersions were determined by dynamic light scattering, and their zeta potentials were measured over a pH range of 5.0–7.5. The crystalline structure and phase composition of the mixed sample were analysed by X-ray diffraction.

An aliquot (1 mL) of each hydrogel precursor solution was transferred into a sample vial and incubated at 37 °C until gelation. The vials were then inverted and photographed to assess macroscopic flow and self-supporting gel formation. To evaluate injectability, the precursor

solutions maintained at 4 °C were loaded into 1 mL syringes and extruded through 21-gauge needles to form letter patterns. Extrusion continuity and pattern retention after gelation were visually assessed. A CS+MoMn hydrogel was selected as a representative sample. After gelation, it was frozen at −80 °C, then freeze-dried to constant weight. A cross-section was prepared and metallized to a thickness of approximately 5 nm, and its internal microstructure was observed using a scanning electron microscope.

Using a rotational rheometer at 37 °C, the storage modulus (G′) and loss modulus (G″) of the hydrogel were measured using a 20-mm-diameter parallel-plate fixture with a 1-mm gap, while an anti-evaporation hood was used to minimize water loss. Separate samples were used for each test, and measurements began after gelation and modulus stabilization. First, a strain sweep from 0.1% to 100% was performed at 1 Hz to determine the linear viscoelastic region. After confirming that a 1% strain fell within the linear viscoelastic region for each group, a frequency sweep from 0.1 to 10 Hz was conducted at a 1% strain, and a 180-second time scan was recorded at 1% strain and 1 Hz. Cyclic step strain tests were performed on the CS+Mn, CS+Mo, and CS+MoMn hydrogels. At 1 Hz, 1% and 100% strains were alternately applied, with each phase lasting 100 s and a total test duration of 700 s. Changes in G′ and G″ during each phase were recorded to evaluate the rheological recovery behavior of the hydrogels. Equal volumes of precursor solution were loaded into 1 mL syringes of the same model fitted with 21 G needles. Using a mechanical testing apparatus, the piston was advanced at a speed of 1 mm/s, and the change in thrust as a function of piston displacement was recorded.

Equal volumes of gelated samples were placed in 5 mL of PBS (pH 7.4) and incubated at 37 °C; separate samples were used at each time point. Degradation experiments were conducted at 0, 1, 3, 7, 14, 21, and 28 h. At 0 h, the initial dry weight was determined using parallel samples from the same batch; at the remaining time points, residual samples were collected, uniformly washed, and freeze-dried to constant weight. Mass loss was evaluated based on the reduction in residual dry weight relative to the initial dry weight. For the swelling experiment, freeze-dried samples with known initial dry weights were immersed in 5 mL of PBS (pH 7.4) and incubated at 37 °C. The samples were removed at 1, 2, 4, 8, 12, 24, 36, 48, and 60 h; surface free water was removed using a consistent method, and the wet weight was then measured. The swelling rate was calculated as the increase in mass due to water absorption relative to the initial dry weight. The dry sample before soaking at 0 h was used as the reference, and the swelling rate was

recorded as 0. For the moisture content experiment, gel-formed hydrogel samples were used. Samples were taken before soaking (0 h) and after soaking at 1, 2, 4, 8, 12, 24, 36, and 48 h. Surface free water was removed using a consistent method, and the wet weight was measured. The samples were then freeze-dried to constant weight, and the moisture content was calculated as the ratio of the mass of water to the wet weight. The degradation, swelling, and moisture content experiments were conducted separately; the same samples were not used for multiple tests.

For the release study, 1 mL of each CS+Mo, CS+Mn, and CS+MoMn precursor solution was transferred into a separate container and allowed to gel at 37 °C. Each gel was then immersed in 2.00 mL of PBS (pH 7.4) or PBS initially containing 0.2 mM H_2O_2 and incubated at 37 °C. Independent samples were prepared for each formulation, medium condition, and collection time point. At 6 and 12 h and on days 1, 3, 5, 7, and 14, the entire release medium surrounding the gel, including suspended particles and spontaneously detached fragments, was collected. The main hydrogel body remaining attached to the container was not scraped or mechanically disrupted. The recovered medium volume was recorded before subsequent analysis. Three independent samples were analyzed at each time point. Samples were processed using an acid digestion procedure capable of completely digesting Mo^0 and α-MnO2, followed by ICP–MS analysis to determine the total Mo and total Mn concentrations in the medium, with results expressed in μg/mL. The Mo concentration was measured in the CS+Mo group, the Mn concentration in the CS+Mn group, and both Mo and Mn concentrations in the CS+MoMn group.

For the cell-free GSH depletion assay, 100 μL of each of the four precursor solutions was taken; after forming a hydrogel at 37 °C, 1.00 mL of freshly prepared 100 μM GSH solution was added, with PBS (pH 7.4) serving as the reaction medium. The samples were incubated at 37 °C in the dark without the addition of H_2O_2. The remaining GSH concentration was measured at 0, 0.5, 1, 2, 4, and 24 h; three independent reaction samples were prepared for each time point. At 0 h, the initial concentration was determined using the GSH reaction solution prior to sample addition. Residual GSH was detected using the DTNB colorimetric method. A 100 μL aliquot of the sample reaction mixture was mixed with 100 μL of phosphate detection buffer (pH 8.0) containing 0.4 mM DTNB, allowed to react at room temperature in the dark for 30 min, and the absorbance was measured at 412 nm. For each assay, standard solutions containing 0, 20, 40, 60, 80, 100, and 120 μM GSH were prepared simultaneously. The standard solutions and samples

underwent the same colorimetric procedure, with the standard concentrations labeled as the concentrations prior to the addition of DTNB. After background correction, the concentration of residual GSH in the reaction solution was calculated based on the standard curve.

For the cell-free H_2O_2-consumption assay, an aliquot (100 μL) of each of the four hydrogel precursor solutions was transferred into a separate container and allowed to gel at 37 °C. Each gel was then incubated with 1.00 mL of freshly prepared 0.2 mM H_2O_2 in PBS (pH 7.4) at 37 °C. Independent reaction samples were prepared for each formulation and time point. The remaining H_2O_2 concentration was measured at 0, 5, 15, 30, 60, and 120 min. The freshly prepared H_2O_2-containing reaction medium collected before exposure to the hydrogels served as the 0-min sample. Residual H_2O_2 was quantified using the Amplex Red/horseradish peroxidase (HRP) assay. At each time point, the reaction medium was diluted 20-fold with the assay reaction buffer. Subsequently, 50 μL of the diluted sample was mixed with 50 μL of working solution containing 100 μM Amplex Red and 0.2 U/mL HRP. The mixture was incubated at room temperature in the dark for 30 min, after which fluorescence was measured at excitation and emission wavelengths of 530 and 590 nm, respectively. H_2O_2 standards of 0, 0.5, 1, 2, 4, 6, 8, and 10 μM were prepared and analyzed using the same procedure. Following background correction, the residual H_2O_2 concentration in the original reaction medium was calculated from the standard curve after accounting for the 20-fold dilution factor. Three independent samples were analyzed for each formulation at every time point.

2.5 Cell culture, hydrogel exposure, and viability assessment

The human clear cell renal cell carcinoma cell lines 786-O and A498 and the immortalized human renal proximal tubular epithelial cell line HK-2 were obtained from the American Type Culture Collection (ATCC). All cell lines were authenticated by short tandem repeat profiling and routinely tested for mycoplasma contamination. 786-O, A498, and HK-2 cells were cultured in RPMI-1640, Eagle's Minimum Essential Medium, and DMEM/F12, respectively, each supplemented with 10% fetal bovine serum. Cells were maintained at 37 °C in a humidified atmosphere containing 5% CO_2. To prepare hydrogel-conditioned media, 0.1 g of each hydrogel formulation was incubated in 1 mL of the corresponding culture medium for 24 h. Following centrifugation, the supernatants were collected and mixed with fresh complete medium at a 1:1

(v/v) ratio for cell treatment. The four formulation groups were Control, CS+Mn, CS+Mo, and CS+MoMn, with Control denoting the nanoparticle-free CS/β-GP hydrogel. Cell viability was assessed using a Cell Counting Kit-8 (CCK-8) assay after 48 h of exposure to the diluted hydrogel-conditioned media. CCK-8 reagent was added according to the manufacturer's instructions, followed by incubation at 37 °C. Absorbance was measured at 450 nm using a microplate reader, and cell viability was expressed relative to the Control group. Three independent biological replicates were performed for each condition, with at least three technical wells per biological replicate. Measurements from technical wells were averaged within each independent culture batch to yield one value per biological replicate for statistical analysis.

2.6 Morphology, membrane integrity, and functional assays

Cytoskeletal staining: Cytoskeletal organization in HK-2 and 786-O cells was examined after 24 h of hydrogel exposure. Cells were washed with phosphate-buffered saline (PBS), fixed with 4% paraformaldehyde for 15 min, and washed three times with PBS for 5 min each. Cells were permeabilized with 0.1% Triton X-100 for 3 min, washed with PBS, and incubated with fluorescently labeled phalloidin for 1 h at room temperature in the dark. Nuclei were counterstained with DAPI for 1 min. After washing, coverslips were mounted, and images were acquired using a fluorescence microscope equipped with a 20× objective. **Live/dead staining:** Cell viability and membrane integrity in HK-2 and 786-O cultures were assessed using Calcein-AM/propidium iodide (PI) staining. Following the indicated treatments, cells were washed once with PBS and incubated with 200 μL of Calcein-AM/PI working solution per well at 37 °C for 30 min in the dark. The staining solution was removed, prewarmed complete culture medium was added, and cells were incubated at 37 °C for a further 30 min. Cells were then washed once with PBS and imaged using a fluorescence microscope equipped with a 20× objective. Calcein-AM-positive cells exhibited green fluorescence, whereas PI-positive cells exhibited red fluorescence.

Scratch-wound migration assay: The migration capacity of 786-O cells was evaluated using a scratch-wound assay. Cells were cultured to approximately 80–90% confluence, and a uniform linear scratch was generated using a sterile pipette tip held perpendicular to the plate surface. Detached cells were removed by washing with PBS. Cells were subsequently maintained in

serum-free medium under the respective indirect hydrogel-exposure conditions described above. Images were acquired immediately after scratching (0 h) and at 12 and 24 h using a bright-field microscope equipped with a 4× objective. The same microscopic fields were imaged at each time point to assess wound closure. **Transwell migration assay:** The migration capacity of 786-O cells was also evaluated using Transwell inserts with 8-μm pores (Corning, 3422) in 24-well plates. Cells were serum-starved overnight, washed once with PBS, and detached using 0.25% trypsin at 37 °C for 1 min. Trypsinization was terminated by adding complete culture medium. The cell suspension was centrifuged at 1500 rpm for 5 min, and the collected cells were resuspended in serum-free medium. Subsequently, 200 μL of the cell suspension was added to the upper chamber, and 600 μL of complete culture medium was added to the lower chamber, ensuring that no air bubbles were trapped beneath the membrane. After incubation at 37 °C for 24 h, the medium was removed, and the inserts were washed with PBS. Nonmigrated cells on the upper membrane surface were gently removed using a cotton swab. Cells on the lower membrane surface were fixed with 4% paraformaldehyde for 15 min, washed three times with PBS, and stained with crystal-violet working solution for 10–15 min. The inserts were washed three times with purified water and air-dried. Images were acquired using a bright-field microscope equipped with a 10× objective from five predefined fields per insert: the center and the upper, lower, left, and right regions. **Post-treatment regrowth and crystal-violet staining:** HK-2 and 786-O cells were exposed to the indicated hydrogel treatments for 24 h. The treatments were then removed, and cells were allowed to recover for 10 days. At the end of the recovery period, the culture medium was removed, and cells were washed once with PBS. Cells were fixed with 4% paraformaldehyde for 15 min, washed three times with PBS for 5 min each, and stained with crystal-violet working solution for 10 min at room temperature. Excess staining solution was removed, and the cultures were rinsed once or twice with purified water. Representative images were acquired using a bright-field microscope equipped with a 4× objective. **H_2O_2 challenge and intracellular ROS assay in HK-2 cells:** HK-2 cells were exposed to 200 μM H_2O_2 for 24 h with or without the indicated hydrogel treatments. Intracellular ROS accumulation was assessed using DCFH-DA. After treatment, cells were washed once with PBS and incubated with 200 μL of DCFH-DA working solution per well at 37 °C for 30 min in the dark. The probe solution was then removed, and cells were washed with PBS before imaging by fluorescence microscopy.

2.7 Oxidative stress and ferroptosis assays

Oxidative stress and ferroptosis-associated responses were evaluated using complementary biochemical, molecular, and pharmacological approaches [20,25]. Intracellular reactive oxygen species (ROS) were assessed using DCFH-DA. Following the indicated treatments, cells were washed once with PBS and incubated with 200 μL of DCFH-DA working solution per well at 37 °C for 30 min in the dark. The staining solution was removed, and cells were washed with PBS. Fluorescence was measured using a microplate reader, and representative images were acquired using a fluorescence microscope equipped with a 20× objective. Lipid peroxidation was assessed using C11-BODIPY 581/591, with fluorescence measured using a microplate reader. Intracellular glutathione levels and the GSH/GSSG ratio were determined using a commercial GSH and GSSG assay kit, and malondialdehyde content was measured using a commercial lipid-peroxidation assay kit, according to the manufacturers' instructions. Intracellular labile Fe^{2+} was assessed using FerroOrange. These biochemical assays were performed in the cell lines specified for the corresponding experiments.

SLC7A11 and GPX4 were examined by immunofluorescence in 786-O cells. Following treatment, cells were washed with PBS, fixed with 4% paraformaldehyde for 15 min, and washed three times with PBS for 5 min each. Cells were permeabilized with 0.2% Triton X-100 for 3 min, washed with PBS, and blocked with 5% bovine serum albumin for 1 h. Cells were incubated with the primary antibodies overnight at 4 °C, washed three times with PBS, and incubated with the corresponding fluorescent secondary antibodies for 1 h. Nuclei were counterstained with DAPI for 1 min. After washing, coverslips were mounted, and fluorescence images were acquired using a 20× objective. SLC7A11 and GPX4 were visualized in red and green, respectively, using the antibody combinations specified in Section 2.1.

Phosphatidylserine externalization was assessed using an Annexin V-FITC/PI apoptosis detection kit followed by flow cytometry, and the percentage of Annexin V-positive cells was determined. For pharmacological rescue experiments, CS+MoMn-treated 786-O cells were co-treated with ferrostatin-1, liproxstatin-1, deferoxamine (DFO), or Z-VAD-FMK. Corresponding rescue experiments in A498 cells included ferrostatin-1, liproxstatin-1, and Z-VAD-FMK. Cell viability and lipid ROS were assessed using CCK-8 and C11-BODIPY 581/591, respectively.

ACSL4 was included as a ferroptosis-associated marker in the immunoblotting panel described in Section 2.8 [26–28].

2.8 Immunoblotting and RT-qPCR

At least 1 × 10^6 cells were lysed in RIPA buffer with protease and phosphatase inhibitors, resolved by SDS-PAGE and transferred to PVDF. Membranes were probed for SLC7A11 and GPX4 (α-tubulin loading control), TFRC, ACSL4 and FTH1 (β-actin), 4-hydroxynonenal (GAPDH), NRF2 and HO-1 (α-tubulin), and caspase-3, cleaved PARP, BCL-2 and BAX (α-tubulin). Band intensities were normalised to the corresponding loading control and expressed relative to control.

Total RNA was extracted by using RNAzol® RT kit (Molecular Research Center (MRC), cat. RN190) according to the manufacturer's instructions from 786-O cells following the indicated treatments and reverse transcribed into complementary DNA (cDNA) using the PrimeScript RT Reagent Kit with gDNA Eraser (Takara, RR047A). Quantitative real-time PCR was performed using TB Green Premix Ex Taq II (Takara, RR820A) on a CFX96 Touch real-time PCR system (Bio-Rad). The expression levels of *PTGS2*, *CHAC1*, *HMOX1*, *NQO1*, *ACSL4*, *GPX4*, *SLC7A11,* and *TFRC* were normalized to the reference gene *ACTB* and expressed as fold changes relative to the Control group. Three independent biological replicates were analyzed, with technical-replicate measurements averaged within each independent culture batch before statistical analysis. Statistical comparisons were performed using the corresponding ΔCt values. Methodological reporting was guided by the MIQE 2.0 recommendations [29]. Amplification was performed using an initial denaturation at 95 °C for 30 s, followed by 40 cycles of 95 °C for 5 s and 60 °C for 30 s, with melt-curve analysis performed after amplification. Primer sequences are provided in Table 1.

Table 1. Primer sequences used for RT-qPCR.

Gene	Species	Forward primer (5′→3′)	Reverse primer (5′→3′)
PTGS2	Human	GAATGTTCCACCCGCAGTACA	GCGTTTGCGGTACTCATTAAAA
CHAC1	Human	TTCTGGCAGGGAGACACCTT	GCCTCTCGCACATTCAGGTA
HMOX1	Human	CCAGCAACAAAGTGCAAAGTTC	TCACATGGCATAAAGCCCTACAG
NQO1	Human	GAAGAGCACTGATCGTACTGGC	GGATACTGAAAGTTCGCAGGG
ACSL4	Human	TTCGATTAAGCCCAGAGCCA	GAGGTAATGGTTCCTCAGCTCCT

Gene	Species	Forward primer (5′→3′)	Reverse primer (5′→3′)
GPX4	Human	GAGGCAAGACCGAAGTAAACTAC	CCGAACTGGTTACACGGGAA
SLC7A11	Human	GGTCCTATTACCAGCTTTTGTACG	AATGTAGCGTCCAAATGCCAG
TFRC	Human	CAGCCCAGCAGAAGCATT	CCAAGAACCGCTTTATCCAG
ACTB	Human	CGGGACCTGACTGACTACCTC	CCATCTCTTGCTCGAAGTCCAG

2.9 Animal experiments

The animal study protocol was reviewed and approved by the Animal Research Ethics Committee of Nanjing Medical University (protocol code IACUC-2109025), and all experiments were reported in accordance with ARRIVE 2.0 [30]. Female BALB/c nude mice aged 3–4 months were purchased from Beijing Vital River Laboratory Animal Technology Co., Ltd. (Charles River, Beijing, China). Mice received subcutaneous 786-O tumors. Once tumors reached the preset volume, animals received a single 50 μL intratumoral injection of the assigned material under inhalational isoflurane anesthesia (RWD Life Science, Shenzhen, China; catalogue no. R510-22-16; 4% for induction and 1.5% for maintenance). A fine needle was advanced into the center of the established tumor mass, the cold sol was deposited as the needle was withdrawn along the track, and the material was allowed to gel in situ at body temperature. No tissue was resected during treatment. Animals were randomized in blocks stratified by pretreatment tumor volume. Injection, image quantification, and pathology scoring were performed by separate operators, each blinded to group allocation. At the study endpoint, mice were euthanized by intraperitoneal injection of an overdose of sodium pentobarbital (200 mg/kg body weight; Sigma-Aldrich/Merck; catalogue no. P3761). Final tumor volume, final tumor weight, and tumor-growth rate were recorded at the endpoint. The individual animal served as the experimental unit, with four animals per group.

2.10 Histology and tissue analysis

Tumors excised at endpoint were fixed, paraffin-embedded and sectioned. Proliferation was assessed by Ki-67 immunohistochemistry, cell death by TUNEL, and necrotic area by haematoxylin and eosin. Heart, liver, spleen, lung and kidney were harvested from all groups and examined by haematoxylin and eosin for treatment-related lesions.

2.11 Haematology, serum chemistry and elemental biodistribution

Whole blood was analysed for haematocrit, haemoglobin, lymphocyte percentage, mean corpuscular haemoglobin concentration, mean corpuscular volume, platelet count, erythrocyte count and leucocyte count. Serum was analysed for alanine aminotransferase, aspartate aminotransferase, urea and total protein. Molybdenum and manganese were quantified by ICP-MS after acid digestion of the injected tumor, of distal organs and of brain tissue, with results normalised to wet tissue mass. Residual hydrogel at the injection site was measured as a percentage of the area originally injected.

2.12 Statistical analysis

Independent culture batches served as biological replicates, and technical replicates were averaged to generate one value for each biological replicate. Unless otherwise indicated, experiments were performed using three independent biological replicates. Comparisons involving one independent factor were performed using one-way analysis of variance (ANOVA), whereas experiments involving two independent factors were analyzed using two-way ANOVA. Tukey's multiple-comparisons test was used for post hoc comparisons. RT–qPCR results were expressed as fold changes relative to the Control group, while statistical analyses were performed using the corresponding ΔCt values. Data are presented as the mean ± standard deviation (SD), and the replicate number is specified in each figure legend. Statistical significance is indicated as $*p < 0.05$, $**p < 0.01$, $***p < 0.001$, and $****p < 0.0001$; ns indicates no significant difference.

3. Results

3.1 The combined α-MnO_2/Mo^0 preparation exhibits particle association and pH-dependent negative surface charge

Because the biological performance of the composite hydrogel depends on the physicochemical properties and compatibility of its inorganic components, we first characterized α-MnO_2, Mo^0, and their combined preparation before evaluating hydrogel formation and biological activity. Transmission electron microscopy revealed discrete, approximately spherical particles in the α-MnO_2, Mo^0, and combined preparations (Figure 1A). Energy-dispersive X-ray spectroscopy showed broadly distributed O, Mn, and C signals within the combined preparation, whereas Mo was not clearly resolved under the applied measurement conditions (Figure 1B). Consistently, the XPS survey spectrum was dominated by O, Mn, and C, with only a weak Mo signal (Figure

1C). High-resolution analysis of the O 1s region provided information on the oxygen-containing chemical environments within the preparation (Figure 1D), while the Mn 2p spectrum was consistent with Mn predominantly existing in the Mn(IV) state characteristic of MnO_2 (Figure 1E). The C 1s spectrum further confirmed the presence of carbon-containing surface components (Figure 1F).

FTIR spectroscopy showed the characteristic polysaccharide- and metal–oxygen-associated bands of the combined preparation, although no distinct Mo-specific vibration was resolved (Figure 1G). Dynamic light scattering revealed mean hydrodynamic diameters of approximately 160 nm for α-MnO_2 and 55 nm for Mo^0, whereas the combined preparation exhibited a larger hydrodynamic diameter of approximately 250 nm (Figure 1H). This increase suggests association between α-MnO_2 and Mo^0 rather than their simple coexistence as two independent particle populations in suspension.

X-ray diffraction confirmed the crystalline α-MnO_2 phase, whereas no independent diffraction peak attributable to Mo^0 was detected in the combined preparation (Figure 1I). Finally, ζ-potential measurements showed that all three preparations remained negatively charged across pH 5.0–7.5 and became progressively more negative as the pH increased (Figure 1J). At pH 7.5, the ζ-potentials of α-MnO_2, Mo^0, and the combined preparation were approximately −27, −14, and −21 mV, respectively, demonstrating pH-dependent changes in particle surface charge.

Collectively, the increased hydrodynamic size and intermediate surface charge of the combined preparation support an association between α-MnO_2 and Mo^0 and indicate physicochemical properties suitable for subsequent incorporation into the polymer network. The weak or unresolved Mo signals obtained by EDS, XPS, XRD, and FTIR are consistent with its comparatively low abundance in the combined formulation and should be considered when interpreting comparisons among the individual-particle and composite groups.

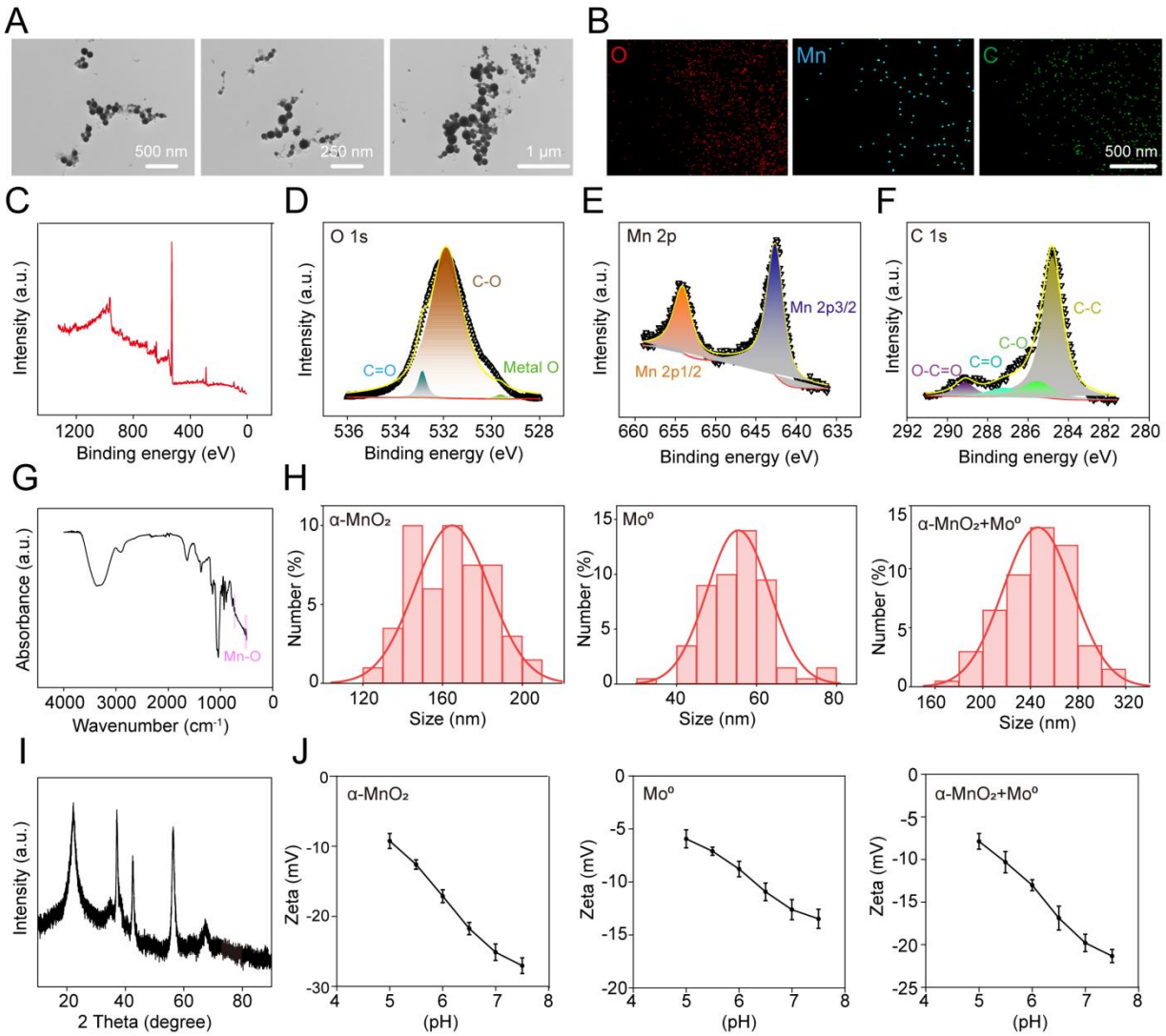


Figure 1. The combined α-MnO_2/Mo^0 preparation exhibits an increased hydrodynamic size and pH-dependent negative surface charge. (A) Representative TEM images showing discrete, approximately spherical particles in the α-MnO_2, Mo^0, and combined preparations. **(B)** EDS elemental maps of the combined preparation showing the spatial distributions of O, Mn, and C; Mo was not clearly resolved under the applied measurement conditions. **(C)** XPS survey spectrum showing predominant C, O, and Mn signals and a comparatively weak Mo signal. **(D–F)** High-resolution O 1s **(D)**, Mn 2p **(E)**, and C 1s **(F)** spectra characterizing the surface chemical environments of the combined preparation. The Mn 2p spectrum was consistent with Mn predominantly existing in the Mn(IV) state. **G,** FTIR spectra showing the characteristic polysaccharide- and metal–oxygen-associated bands of the individual and combined preparations, without a clearly resolved Mo-specific vibration. **(H)** Hydrodynamic size distributions measured by dynamic light scattering. The approximate mean diameters were 160 nm for α-MnO_2, 55 nm for Mo^0, and 250 nm for the combined preparation; the increased size of the combined preparation supports particle association. **(I)** XRD patterns confirming the crystalline α-MnO_2 phase, whereas no independent Mo^0 diffraction peak was resolved in the combined preparation. **(J)** ζ-potential profiles measured over pH 5.0–7.5. All preparations remained negatively charged and became progressively more negative with increasing pH, reaching approximately −27, −14, and −21 mV for α-MnO_2, Mo^0, and the combined preparation, respectively, at pH 7.5.

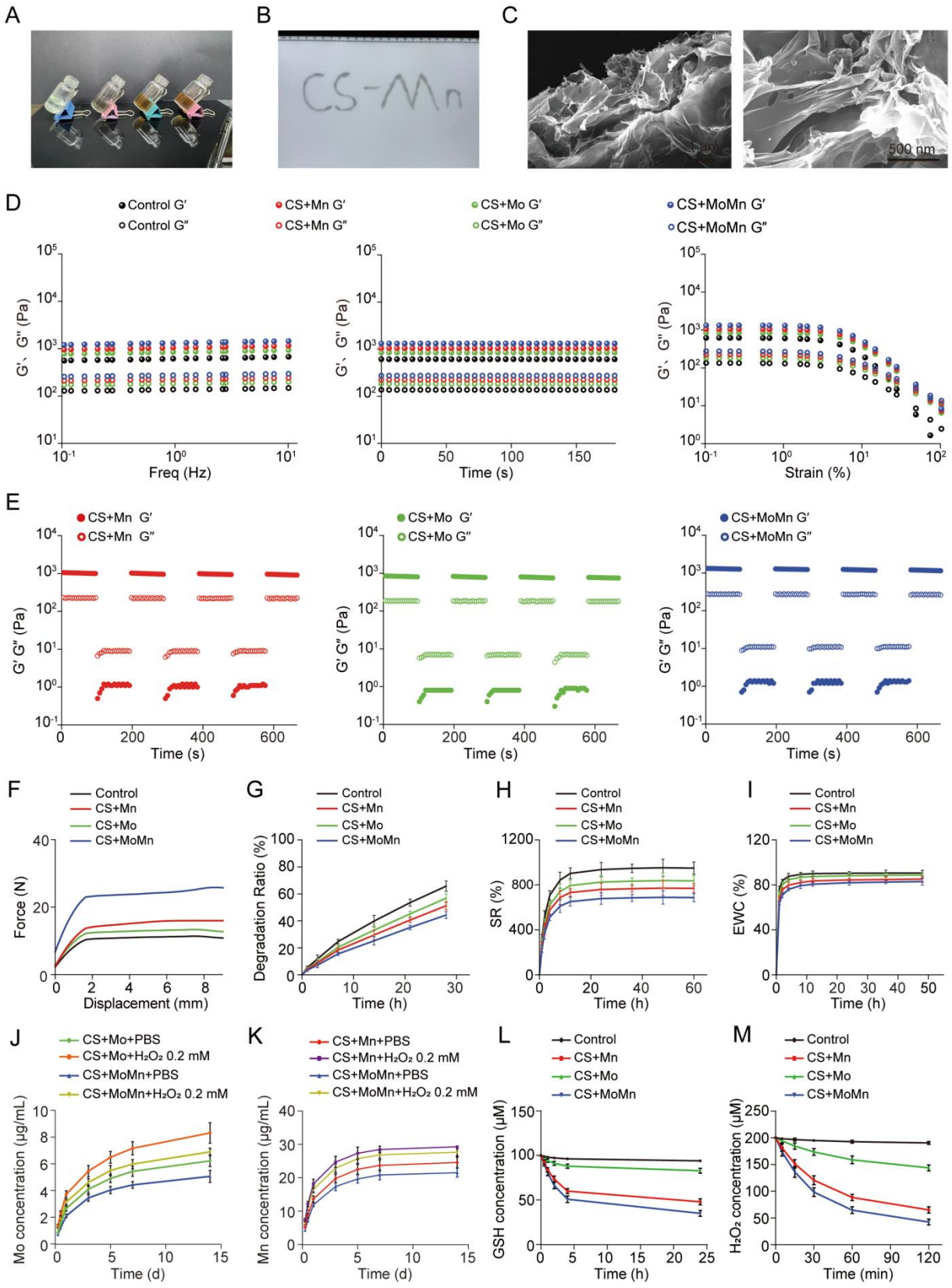
3.2 CS+MoMn forms an injectable, porous, self-recovering gel with oxidation-enhanced Mo and Mn release

All four CS/β-GP hydrogel formulations retained their gelled state upon vial inversion, and a representative formulation could be extruded into a continuous lettering pattern, demonstrating its injectability (Figure 2A,B). SEM images revealed a porous internal structure (Figure 2C). Rheological measurements showed that the storage modulus (G′) exceeded the loss modulus (G″) across the tested frequency range and time window for all formulations, with CS+MoMn exhibiting the highest overall G′. Both moduli decreased with increasing strain. During alternating low- and high-strain cycles, the particle-loaded hydrogels recovered their moduli to approximately their initial levels upon returning to low strain, demonstrating rheological recovery (Figure 2D,E). The injection force–displacement curves showed that CS+MoMn required a greater plunger force at the same displacement than the other formulations, indicating greater resistance during extrusion through the needle (Figure 2F).

The degradation percentage increased over time for all formulations and was comparatively lower in the CS+MoMn group (Figure 2G). The swelling ratio and water content increased rapidly during the initial stage and subsequently approached a plateau. CS+MoMn exhibited a lower swelling ratio and lower plateau water content than the other formulations (Figure 2H,I). Thus, the co-loaded hydrogel exhibited a higher elastic response, reduced water uptake, and lower dry-mass loss under the tested conditions. Mo and Mn concentrations in the release media increased over time, with a relatively rapid initial increase followed by progressively smaller increments (Figure 2J,K). Compared with PBS alone, PBS supplemented with an initial H_2O_2 concentration of 0.2 mM yielded higher elemental concentrations in the corresponding groups. Under the same medium conditions, Mo and Mn concentrations released from CS+MoMn were lower than those from the respective single-component formulations.

Cell-free measurements showed that the remaining GSH concentration decreased with incubation time in the particle-loaded hydrogel groups. CS+MoMn exhibited the lowest remaining GSH concentration, followed by CS+Mn, whereas CS+Mo showed a smaller decrease and the unloaded control showed limited changes (Figure 2L). The remaining H_2O_2 concentration exhibited a similar group-dependent pattern, with the greatest decrease in CS+MoMn, followed

by CS+Mn and CS+Mo, while the control remained relatively stable (Figure 2M). Under the tested conditions, the co-loaded formulation produced greater reductions in GSH and H_2O_2 concentrations than the corresponding single-component formulations.


A
B
CS-Mn
C
500 nm
D
Control G′
Control G″
CS+Mn G′
CS+Mn G″
CS+Mo G′
CS+Mo G″
CS+MoMn G′
CS+MoMn G″
G′、G″ (Pa)
Freq (Hz)
Time (s)
Strain (%)
E
CS+Mn G′
CS+Mn G″
CS+Mo G′
CS+Mo G″
CS+MoMn G′
CS+MoMn G″
G′ G″ (Pa)
Time (s)
F
Control
CS+Mn
CS+Mo
CS+MoMn
Force (N)
Displacement (mm)
G
Degradation Ratio (%)
Time (h)
H
SR (%)
Time (h)
I
EWC (%)
Time (h)
J
CS+Mo+PBS
CS+Mo+H₂O₂ 0.2 mM
CS+MoMn+PBS
CS+MoMn+H₂O₂ 0.2 mM
Mo concentration (μg/mL)
Time (d)
K
CS+Mn+PBS
CS+Mn+H₂O₂ 0.2 mM
CS+MoMn+PBS
CS+MoMn+H₂O₂ 0.2 mM
Mn concentration (μg/mL)
Time (d)
L
GSH concentration (μM)
Time (h)
M
H₂O₂ concentration (μM)
Time (min)

544

Figure 2. Physicochemical characterization, elemental release, and cell-free redox activity of Mo^0/α-MnO2-loaded CS/β-GP hydrogels. **(A)** Representative photographs showing gel formation of the four formulations assessed by vial inversion. **(B)** Demonstration of hydrogel injectability by extrusion into a lettering pattern. **(C)** Scanning electron microscopy images of the hydrogel microstructure at different magnifications. **(D)** Storage modulus (G′) and loss modulus (G″) of the four formulations during frequency sweeps, time sweeps, and strain sweeps, respectively. **(E)** Changes in G′ and G″ during alternating low- and high-strain cycles for CS+Mn, CS+Mo, and CS+MoMn hydrogels. **(F)** Injection force – displacement curves of the four formulations. **G,** Hydrogel degradation profiles. **(H)** Swelling ratio (SR). **(I)** Equilibrium water content (EWC) over time. **(J)** Mo concentrations in release media containing PBS alone or PBS supplemented with an initial H_2O_2 concentration of 0.2 mM. **(K)** Mn concentrations in release media containing PBS alone or PBS supplemented with an initial H_2O_2 concentration of 0.2 mM. **(L)** Remaining GSH concentrations over time following incubation with the four hydrogel formulations in a cell-free system. **(M)** Remaining H_2O_2 concentrations over time following incubation with the four formulations in a cell-free system, starting from 0.2 mM H_2O_2. Data are presented as mean ± SD (n = 3).

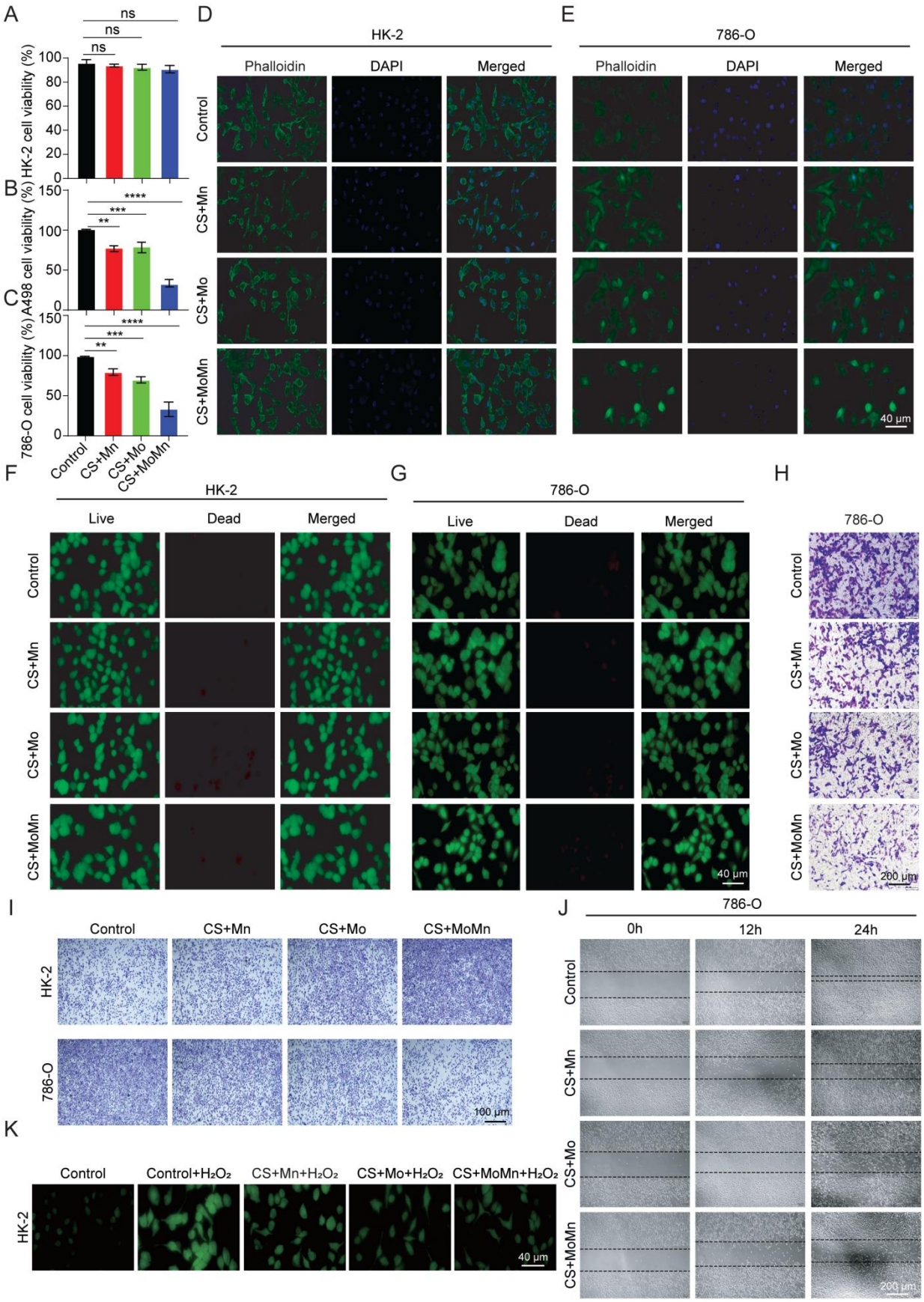
3.3 CS+MoMn preferentially suppresses ccRCC cell viability and regrowth while preserving HK-2 cells

Because a locally administered antitumor hydrogel should suppress malignant cells without substantially injuring the surrounding renal epithelium, we compared the responses of two ccRCC cell lines, A498 and 786-O, with those of HK-2 renal tubular epithelial cells under matched treatment conditions. After 48 h of exposure, HK-2 cell viability remained largely unchanged, decreasing from approximately 97% in the Control to 95%, 94%, and 92% following CS+Mn, CS+Mo, and CS+MoMn treatment, respectively (Figure 3A). In contrast, A498 viability was reduced by both single-particle formulations and decreased to approximately 35% following CS+MoMn treatment (Figure 3B). Similarly, 786-O viability decreased progressively to approximately 79%, 69%, and 30% following CS+Mn, CS+Mo, and CS+MoMn treatment, respectively (Figure 3C). Thus, the dual-particle formulation markedly reduced the viability of both ccRCC cell lines while producing only a limited, nonsignificant change in HK-2 viability. Consistent with the viability results, HK-2 cells maintained a spread morphology and relatively organized F-actin architecture following the different treatments (Figure 3D). By contrast, phalloidin staining of 786-O cells revealed progressive loss of cell spreading and cytoskeletal organization, with CS+MoMn-treated cells exhibiting the most pronounced rounding and actin condensation or disorganization (Figure 3E). Live/dead staining further showed that HK-2 cultures remained predominantly Calcein-AM-positive, with only limited PI-positive staining across the treatment groups (Figure 3F). In comparison, 786-O cells exhibited reduced viable-cell density and increased dead-cell staining following treatment with the particle-containing formulations, with the strongest effect observed in the CS+MoMn group (Figure 3G). These

findings further support the preferential cytotoxicity of the dual-particle formulation toward ccRCC cells.

Functional assays showed a consistent treatment-dependent response. Representative Transwell images indicated a progressive reduction in migrated 786-O cells across the treatment series, with the lowest cell density observed following CS+MoMn treatment (Figure 3H). Clonogenic cultures obtained after treatment washout and 10 days of recovery showed that HK-2 cells largely retained their colony-forming capacity, whereas 786-O clonogenic regrowth was reduced, particularly in the Mo-containing groups (Figure 3I). Scratch-wound images similarly indicated delayed 786-O wound closure at 12 and 24 h, with the most pronounced inhibition observed following CS+MoMn treatment (Figure 3J). We further examined whether the formulations protected renal epithelial cells against oxidative stress. H_2O_2 challenge markedly increased DCFH-DA fluorescence in HK-2 cells, whereas treatment with the particle-containing hydrogels reduced intracellular ROS accumulation. The strongest reduction was observed following CS+MoMn treatment, for which the fluorescence signal approached that of the Control (Figure 3K). These findings suggest that the dual-particle formulation did not aggravate oxidative injury in HK-2 cells and instead attenuated H_2O_2-induced ROS accumulation under the tested conditions.

Collectively, the reductions in A498 and 786-O cell viability, impaired 786-O migration and clonogenic regrowth, preservation of HK-2 viability and morphology, and attenuation of oxidative stress in HK-2 cells support a preferential antitumor effect of CS+MoMn. These findings suggest that the dual-particle hydrogel can limit both short-term ccRCC-cell survival and post-treatment regrowth while largely preserving the renal tubular epithelial-cell model.


A
B
C
D
E
F
G
H
I
J
K
HK-2 cell viability (%)
A498 cell viability (%)
786-O cell viability (%)
ns
Control
CS+Mn
CS+Mo
CS+MoMn
Phalloidin
DAPI
Merged
Live
Dead
786-O
0h
12h
24h
Control+H₂O₂
CS+Mn+H₂O₂
CS+Mo+H₂O₂
CS+MoMn+H₂O₂
40 μm
200 μm
100 μm

603

Figure 3. CS+MoMn preferentially suppresses ccRCC cells while preserving HK-2 renal tubular epithelial cells. (A–C) Cell viability of HK-2 **(A)**, A498 **(B)**, and 786-O **(C)** cells after 48 h of treatment with the indicated formulations. **(D, E)** Representative phalloidin/DAPI fluorescence images showing F-actin organization in HK-2 **(D)** and 786-O **(E)** cells. **(F, G)** Representative Calcein-AM/PI live/dead staining of HK-2 **(F)** and 786-O **(G)** cells. **(H)** Representative Transwell migration images of 786-O cells. **(I)** Representative crystal-violet-stained clonogenic cultures of HK-2 and 786-O cells following treatment and recovery. **(J)** Representative scratch-wound images of 786-O cells at 0, 12, and 24 h. **(K)** Representative DCFH-DA fluorescence images showing intracellular ROS accumulation in HK-2 cells challenged with 200 μM H_2O_2 and treated with the indicated formulations. Scale bars: 40 μm in **(D–G, K)**, 200 μm in **(H, J)**, and 100 μm in **(I)**. Quantitative data are presented as the mean ± SD of three independent biological experiments (n = 3). Data in **(A–C)** were analyzed using one-way ANOVA followed by Tukey's multiple-comparisons test. ns, not significant; *$p < 0.05$, ** $p < 0.01$, ***$p < 0.001$, and **** $p < 0.0001$.

3.4 CS+MoMn induces lipid peroxidation- and Fe^{2+}-associated cell death that is preferentially rescued by ferroptosis inhibitors

Having established that CS+MoMn preferentially reduced ccRCC-cell viability, we next investigated the mechanism underlying this cytotoxic response. Immunofluorescence imaging indicated reduced SLC7A11 and GPX4 signals following treatment with the particle-containing formulations, with the most pronounced reduction observed in the CS+MoMn group (Figure 4A). Total intracellular ROS increased across the treatment series and was highest following CS+MoMn treatment (Figure 4B). Consistently, C11-BODIPY oxidation increased progressively and reached approximately threefold above the Control level in CS+MoMn-treated 786-O cells, indicating marked lipid peroxidation (Figure 4C). Furthermore, intracellular GSH decreased to approximately 34% of the Control level following CS+MoMn treatment (Figure 4D), accompanied by a pronounced reduction in the GSH/GSSG ratio (Figure 4E). These changes indicate substantial depletion of intracellular reducing capacity. Consistent with the C11-BODIPY results, MDA content and the labile Fe^{2+} pool increased progressively across the treatment groups, reaching their highest levels following CS+MoMn exposure. In the dual-particle group, the labile Fe^{2+} level was approximately 2.2-fold higher than that in the Control (Figure 4F,G). Annexin V positivity also increased from approximately 6% in the Control group to approximately 42% following CS+MoMn treatment, consistent with increased cell death (Figure 4H).

To determine which cell-death pathway contributed functionally to CS+MoMn-induced cytotoxicity, pharmacological rescue experiments were performed using the lipid-radical-trapping agents ferrostatin-1 (Fer-1) and liproxstatin-1 (Lip-1), the iron chelator deferoxamine (DFO), and the pan-caspase inhibitor Z-VAD-FMK. CS+MoMn reduced 786-O cell viability to

approximately 35%. Co-treatment with Fer-1, Lip-1, or DFO substantially restored viability to approximately 67–74%, whereas Z-VAD-FMK produced a smaller recovery to approximately 48% (Figure 4I). The greater protection provided by two chemically distinct ferroptosis inhibitors and an iron chelator than by caspase inhibition supports a major contribution of iron-dependent lipid peroxidation to CS+MoMn-induced cell death.

To determine whether this response extended beyond 786-O cells, key ferroptosis-associated endpoints were examined in A498 cells. CS+MoMn produced the greatest reductions in intracellular GSH and the GSH/GSSG ratio (Figure 4J,K), together with the strongest increases in labile Fe^{2+} and MDA levels (Figure 4L,M). Importantly, the particle-containing formulations did not significantly alter C11-BODIPY oxidation in HK-2 cells (Figure 4N), whereas lipid peroxidation increased markedly in A498 cells and was highest following CS+MoMn treatment (Figure 4O). Pharmacological rescue experiments in A498 cells further showed that Fer-1 and Lip-1 substantially restored cell viability, whereas Z-VAD-FMK provided only partial protection (Figure 4P). These results reproduce the principal biochemical and pharmacological responses observed in 786-O cells and further support preferential ferroptotic stress in ccRCC cells relative to the renal tubular epithelial-cell model.

Collectively, the coordinated depletion of GSH, reduction of the GSH/GSSG ratio, suppression of SLC7A11- and GPX4-associated antioxidant defenses, accumulation of lipid-peroxidation products, expansion of the labile Fe^{2+} pool, and substantial rescue by Fer-1, Lip-1, and DFO provide convergent evidence that ferroptosis makes a major functional contribution to CS+MoMn-induced ccRCC-cell death. The smaller but detectable rescue produced by Z-VAD-FMK suggests that a caspase-dependent mechanism may occur concurrently.

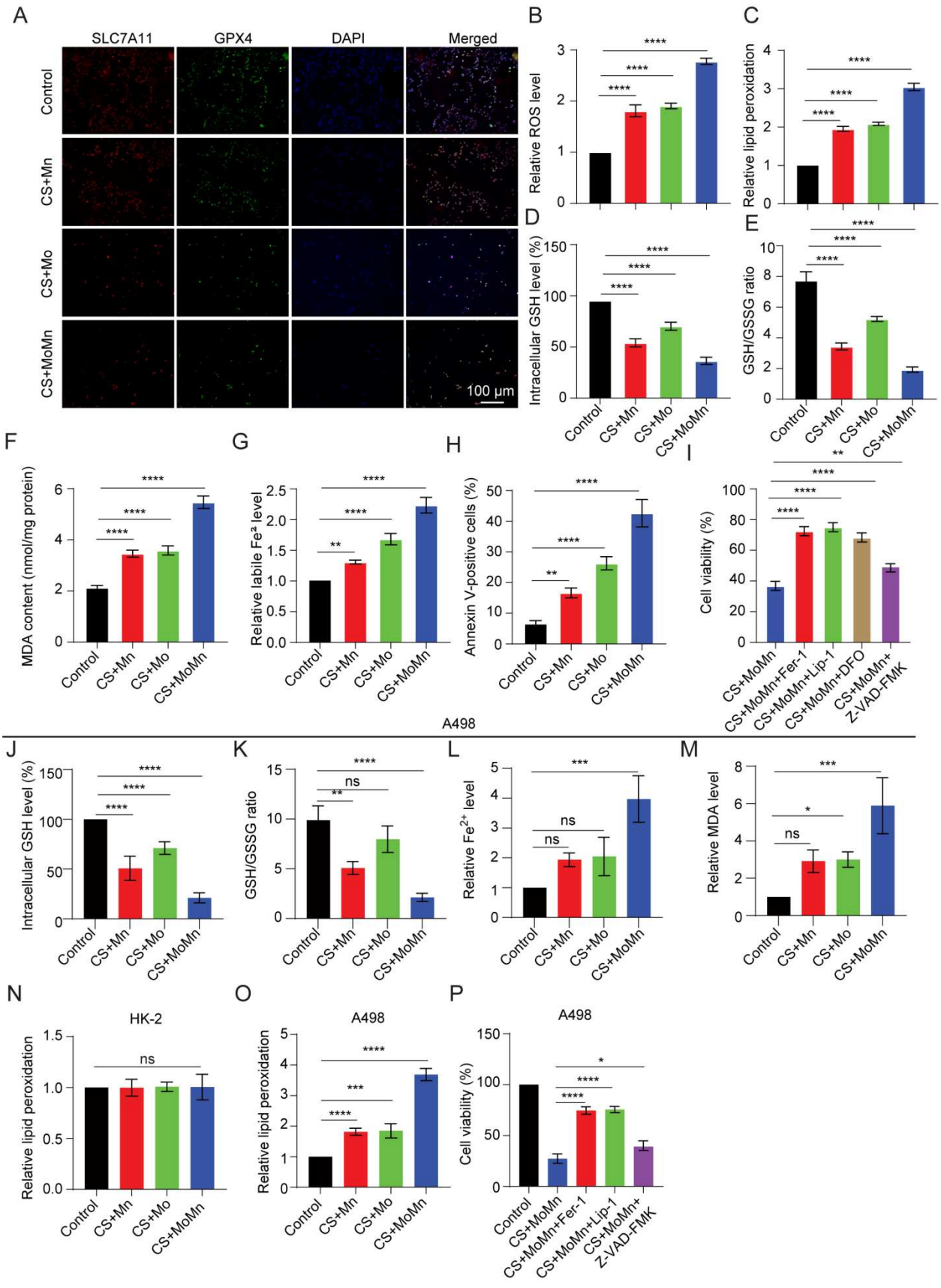

A
SLC7A11
GPX4
DAPI
Merged
Control
CS+Mn
CS+Mo
CS+MoMn
100 μm
B
Relative ROS level
C
Relative lipid peroxidation
D
Intracellular GSH level (%)
E
GSH/GSSG ratio
F
MDA content (nmol/mg protein)
G
Relative labile Fe² level
H
Annexin V-positive cells (%)
I
Cell viability (%)
CS+MoMn
CS+MoMn+Fer-1
CS+MoMn+Lip-1
CS+MoMn+DFO
CS+MoMn+ Z-VAD-FMK
A498
J
Intracellular GSH level (%)
K
GSH/GSSG ratio
L
Relative Fe2+ level
M
Relative MDA level
N
HK-2
Relative lipid peroxidation
O
A498
Relative lipid peroxidation
P
A498
Cell viability (%)
ns

Figure 4. CS+MoMn induces ferroptosis-associated oxidative damage in ccRCC cells and is preferentially rescued by ferroptosis inhibitors. (A) Representative immunofluorescence images of SLC7A11 (red) and GPX4 (green) in 786-O cells following the indicated treatments; nuclei were counterstained with DAPI (blue). **(B, C)** Relative intracellular total ROS levels measured using DCFH-DA **(B)** and lipid peroxidation measured using C11-BODIPY 581/591 **(C)** in 786-O cells. **(D–H)** Intracellular GSH level **(D)**, GSH/GSSG ratio **(E)**, MDA content **(F)**, relative labile Fe^{2+} level **(G)**, and percentage of Annexin V-positive cells **(H)** in 786-O cells. **(I)** Viability of CS+MoMn-treated 786-O cells following co-treatment with ferrostatin-1 (Fer-1), liproxstatin-1 (Lip-1), deferoxamine (DFO), or Z-VAD-FMK. **(J–M)** Intracellular GSH level **(J)**, GSH/GSSG ratio **(K)**, relative labile Fe^{2+} level **(L)**, and relative MDA level **(M)** in A498 cells following the indicated treatments. **(N, O)** Relative lipid peroxidation measured using C11-BODIPY 581/591 in HK-2 **(N)** and A498 **(O)** cells. **(P)** Viability of A498 cells treated with CS+MoMn alone or in combination with Fer-1, Lip-1, or Z-VAD-FMK. Data are presented as the mean ± SD of three independent biological experiments ($n = 3$). Each endpoint was analyzed separately using one-way ANOVA followed by Tukey's multiple-comparisons test. ns, not significant; * $p < 0.05$, ** $p < 0.01$, *** $p < 0.001$, and **** $p < 0.0001$.

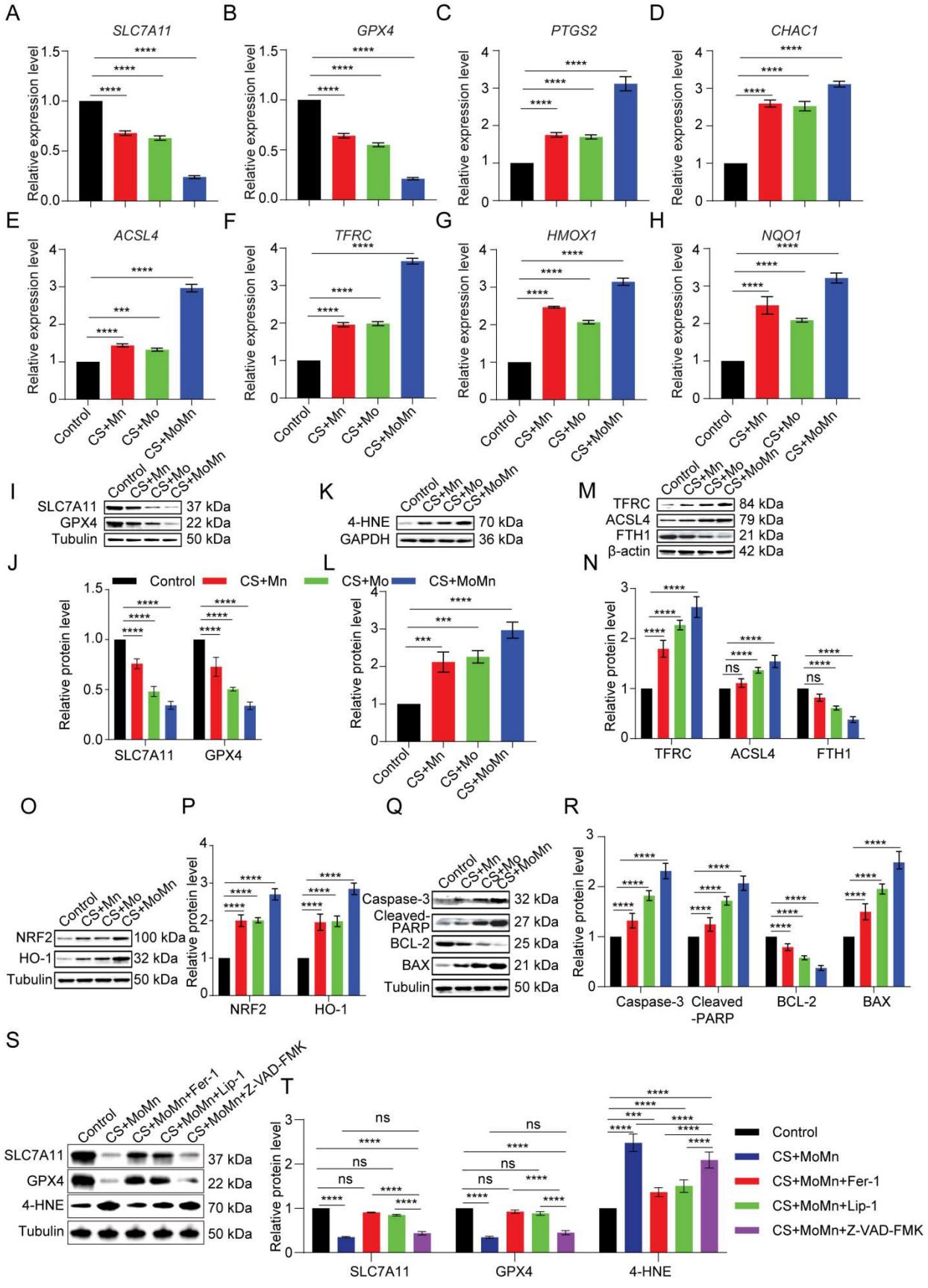
3.5 CS+MoMn suppresses the SLC7A11–GPX4 defense axis and activates ferroptosis-associated molecular programs

To molecularly validate the biochemical and pharmacological evidence in Figure 4, we examined ferroptosis-, oxidative-stress-, iron-metabolism-, and apoptosis-associated markers at the transcript and protein levels. RT–qPCR analysis of 786-O cells showed that CS+MoMn markedly reduced *SLC7A11* and *GPX4* expression while increasing *PTGS2*, *CHAC1*, *ACSL4*, *TFRC*, *HMOX1*, and *NQO1* expression (Figure 5A–H). The dual-particle formulation generally produced the strongest changes, including an approximately threefold increase in *ACSL4* and a three- to fourfold increase in the ferroptosis- and oxidative-stress-associated transcripts. Although *PTGS2* and *CHAC1* are not independently specific for ferroptosis, their induction together with suppression of *SLC7A11* and *GPX4* supports activation of a coordinated ferroptotic-stress response. Western blotting confirmed progressive suppression of SLC7A11 and GPX4, with the lowest abundance observed following CS+MoMn treatment (Figure 5I,J). Consistent with impaired glutathione-dependent lipid-peroxide detoxification, 4-HNE protein adducts increased across the treatment series and reached approximately threefold above the Control level in the dual-particle group (Figure 5K,L). CS+MoMn also increased TFRC and ACSL4 while decreasing FTH1 (Figure 5M,N), indicating increased iron-uptake potential, reduced ferritin-associated iron-storage capacity, and enhanced susceptibility of membrane lipids to peroxidation.

NRF2 and HO-1 abundance also increased, with the strongest responses observed following CS+MoMn treatment (Figure 5O,P). These changes likely represent an adaptive

oxidative-stress response mounted against the extensive redox disturbance rather than a protective effect of the treatment. Apoptosis-associated proteins were altered concurrently: Caspase-3 abundance, cleaved PARP, and BAX increased, whereas BCL-2 decreased (Figure 5Q,R). Together with the partial protection afforded by Z-VAD-FMK, the cleaved-PARP and BAX/BCL-2 changes are consistent with a concurrent apoptosis-associated response [31]. Finally, pharmacological rescue experiments were used to determine whether inhibition of ferroptosis reversed these molecular changes in 786-O cells. Ferrostatin-1 and liproxstatin-1 restored SLC7A11 and GPX4 abundance and reduced 4-HNE accumulation more effectively than Z-VAD-FMK (Figure 5S,T). This molecular rescue pattern is consistent with the viability results and further supports iron-dependent lipid peroxidation as a major contributor to CS+MoMn-induced cytotoxicity.

Collectively, the coordinated suppression of the SLC7A11–GPX4 defense axis, accumulation of 4-HNE, induction of ACSL4 and TFRC, reduction of FTH1, and the reversal by ferroptosis inhibitors provide convergent molecular evidence that ferroptosis makes a major contribution to CS+MoMn-induced ccRCC-cell death. The accompanying caspase/PARP and BAX/BCL-2 responses indicate that apoptosis may occur concurrently as a secondary mechanism.


A
SLC7A11
B
GPX4
C
PTGS2
D
CHAC1
E
ACSL4
F
TFRC
G
HMOX1
H
NQO1
Relative expression level
Control
CS+Mn
CS+Mo
CS+MoMn
I
SLC7A11 37 kDa
GPX4 22 kDa
Tubulin 50 kDa
K
4-HNE 70 kDa
GAPDH 36 kDa
M
TFRC 84 kDa
ACSL4 79 kDa
FTH1 21 kDa
β-actin 42 kDa
J
Relative protein level
L
N
O
NRF2 100 kDa
HO-1 32 kDa
P
Q
Caspase-3 32 kDa
Cleaved-PARP 27 kDa
BCL-2 25 kDa
BAX 21 kDa
R
Caspase-3
Cleaved -PARP
S
CS+MoMn+Fer-1
CS+MoMn+Lip-1
CS+MoMn+Z-VAD-FMK
T
4-HNE
ns

714

Figure 5. CS+MoMn disrupts antioxidant defense and induces ferroptosis- and apoptosis-associated molecular remodeling in ccRCC cells. (A–H) RT–qPCR analysis of *SLC7A11* **(A)**, *GPX4* **(B)**, *PTGS2* **(C)**, *CHAC1* **(D)**, *ACSL4* **(E)**, *TFRC* **(F)**, *HMOX1* **(G)**, and *NQO1* **(H)** expression in 786-O cells following the indicated treatments. Transcript levels were normalized to the reference gene *ACTB* and expressed relative to the Control. **(I, J)** Representative Western blots of SLC7A11 and GPX4 **(I)** and their densitometric quantification **(J)** in 786-O cells. Tubulin was used as the loading control. **(K, L)** Representative Western blot of 4-HNE–protein adducts **(K)** and densitometric quantification **(L)**. GAPDH was used as the loading control. **(M, N)** Representative Western blots of TFRC, ACSL4, and FTH1 **(M)** and their densitometric quantification **(N)**. β-Actin was used as the loading control. **(O, P)** Representative Western blots of NRF2 and HO-1 **(O)** and their densitometric quantification **(P)**. Tubulin was used as the loading control. **(Q, R)** Representative Western blots of caspase-3, cleaved PARP, BCL-2, and BAX **(Q)** and their densitometric quantification **(R)**. Tubulin was used as the loading control. **(S, T)** Representative Western blots of SLC7A11, GPX4, and 4-HNE–protein adducts in CS+MoMn-treated 786-O cells co-treated with ferrostatin-1 (Fer-1), liproxstatin-1 (Lip-1), or Z-VAD-FMK **(S)** and their densitometric quantification **(T)**. Tubulin was used as the loading control in **(S)**. Protein abundance was normalized to the corresponding loading control and expressed relative to the Control. Data are presented as the mean ± SD of three independent biological experiments ($n = 3$). Each endpoint was analyzed separately using one-way ANOVA followed by Tukey's multiple-comparisons test. ns, not significant; * $p < 0.05$, ** $p < 0.01$, *** $p < 0.001$, and **** $p < 0.0001$.

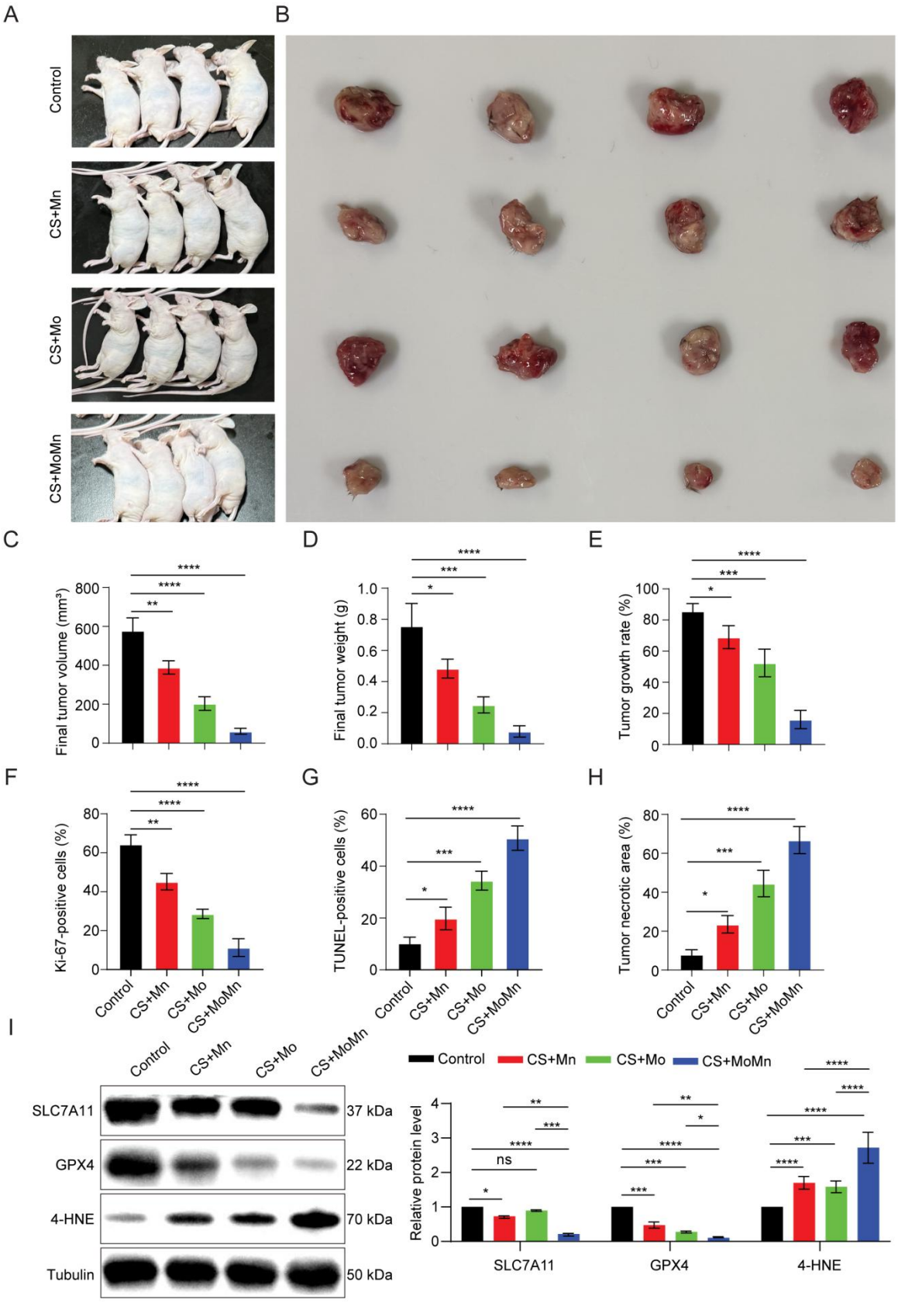
3.6 A single intratumoral dose of CS+MoMn suppresses established subcutaneous tumor growth and induces ferroptosis-associated molecular changes

To determine whether the preferential ccRCC cytotoxicity observed in vitro translated into antitumor activity in vivo, we evaluated the formulations in mice bearing established subcutaneous 786-O tumors. Animals received a single 50 μL intratumoral injection of Control hydrogel, CS+Mn, CS+Mo, or CS+MoMn, with four animals per group. At the study endpoint, representative images of tumor-bearing mice and excised tumors showed a progressive reduction in tumor burden across the treatment groups, with the smallest tumors observed following CS+MoMn treatment (Figure 6A,B). Final tumor volume decreased from approximately 580 mm^3 in the Control group to 375, 205, and 65 mm^3 in the CS+Mn, CS+Mo, and CS+MoMn groups, respectively (Figure 6C). Tumor weight showed the same treatment-dependent pattern, decreasing from approximately 0.75 g in the Control group to 0.41, 0.21, and 0.06 g, respectively (Figure 6D). Consistently, the calculated tumor-growth rate decreased from approximately 85% in the Control group to 65%, 48%, and 14% following CS+Mn, CS+Mo, and CS+MoMn treatment, respectively (Figure 6E). These three tumor-growth endpoints consistently identified CS+MoMn as the most effective formulation among the tested groups.

Quantitative tissue analyses further supported the macroscopic antitumor response. Ki-67 positivity decreased progressively from approximately 64% in the Control group to 11% following CS+MoMn treatment, indicating marked suppression of tumor-cell proliferation (Figure 6F). Conversely, TUNEL positivity increased from approximately 9% to 50%, consistent

with enhanced treatment-associated DNA fragmentation and cell death (Figure 6G). Tumor necrotic area also increased from approximately 6% in the Control group to 62% in the CS+MoMn group, demonstrating extensive tumor-tissue damage following dual-particle treatment (Figure 6H). Western blot analysis of tumor tissues showed progressive reductions in SLC7A11 and GPX4 abundance, accompanied by increased accumulation of 4-HNE–protein adducts, with the most pronounced changes observed in the CS+MoMn group (Figure 6I). These molecular changes indicate impaired glutathione-dependent lipid-peroxide defense and enhanced lipid-peroxidative stress within the treated tumors, consistent with the ferroptosis-associated responses observed in vitro.

Collectively, the reductions in tumor volume, tumor weight, calculated tumor-growth rate, and Ki-67 positivity, together with increased TUNEL positivity, tumor necrosis, and ferroptosis-associated molecular changes, demonstrate that a single intratumoral administration of CS+MoMn produced the strongest suppression of established subcutaneous tumor growth among the tested formulations.


A
B
Control
CS+Mn
CS+Mo
CS+MoMn
C
Final tumor volume (mm³)
D
Final tumor weight (g)
E
Tumor growth rate (%)
F
Ki-67-positive cells (%)
G
TUNEL-positive cells (%)
H
Tumor necrotic area (%)
Control
CS+Mn
CS+Mo
CS+MoMn
I
SLC7A11
GPX4
4-HNE
Tubulin
37 kDa
22 kDa
70 kDa
50 kDa
Relative protein level
ns

766

Figure 6. A single intratumoral administration of CS+MoMn suppresses established subcutaneous tumor growth and produces ferroptosis-associated molecular changes. (A) Representative photographs of tumor-bearing mice from the Control, CS+Mn, CS+Mo, and CS+MoMn groups at the study endpoint. **(B)** Gross images of tumors excised from all animals at the endpoint. **(C, D)** Final tumor volume **(C)** and tumor weight **(D)**. **(E)** Calculated tumor-growth rate at the study endpoint. **(F–H)** Quantification of Ki-67-positive cells **(F)**, TUNEL-positive cells **(G)**, and tumor necrotic area **(H)**. **(I)** Representative Western blots and densitometric quantification of SLC7A11, GPX4, and 4-HNE in tumor tissues. Tubulin was used as the loading control. Data are presented as the mean ± SD (n = 4 animals per group). Each endpoint was analyzed separately using one-way ANOVA followed by Tukey's multiple-comparisons test. ns, not significant; * $p < 0.05$, ** $p < 0.01$, *** $p < 0.001$, and **** $p < 0.0001$.

3.7 Intratumoral CS+MoMn shows favorable short-term systemic tolerability and tumor-enriched Mo/Mn accumulation

Because intratumoral delivery is intended to concentrate therapeutic activity within the tumor while limiting systemic exposure, we evaluated major-organ histology, hematological and serum biochemical parameters, elemental biodistribution, and local hydrogel retention at the study endpoint. H&E staining of the heart, liver, spleen, lungs, and kidneys showed preserved tissue architecture without overt treatment-associated lesions, extensive necrosis, or inflammatory infiltration in any group (Figure 7A). Consistent with the histological findings, no significant differences were detected among the groups in the evaluated hematological parameters, including hematocrit, hemoglobin, lymphocyte percentage, mean corpuscular hemoglobin concentration, mean corpuscular volume, platelet count, red blood cell count, and white blood cell count (Figure 7B–I). Serum biochemical indices, including alanine aminotransferase, aspartate aminotransferase, urea, and total protein, also remained comparable among the groups (Figure 7J–M). These results indicate that a single intratumoral administration did not produce detectable short-term alterations in the evaluated hematological, hepatic, or renal indices.

ICP–MS analysis showed treatment-dependent elemental accumulation within the injected tumors. Tumor Mo concentrations increased in the CS+Mo and CS+MoMn groups, whereas tumor Mn concentrations increased in the CS+Mn and CS+MoMn groups. The highest tumor-associated concentrations of both elements were detected following administration of the dual-particle formulation (Figure 7N,O). In comparison, the mean Mo concentration across the analyzed distal organs remained markedly lower than that measured in the injected tumors, although modest increases were detected in the Mo-containing groups (Figure 7P). These findings indicate tumor-enriched rather than exclusively tumor-confined Mo accumulation.

Mn was measurable in brain tissue from all groups, consistent with its physiological presence as an essential trace element. Nevertheless, the highest brain Mn concentration was detected in the CS+MoMn group, indicating that a fraction of the administered Mn reached distal tissue (Figure 7Q). Residual hydrogel remained detectable at the injection site on day 14 in the particle-loaded groups, with the greatest residual area observed for CS+MoMn (Figure 7R). This local retention may support prolonged residence of the incorporated particles and sustained exposure of the tumor to the therapeutic components.

Collectively, the absence of overt major-organ histopathology and significant hematological or biochemical alterations supports favorable short-term systemic tolerability under the tested conditions. The biodistribution data further demonstrate tumor-enriched Mo and Mn accumulation together with persistent local hydrogel retention.

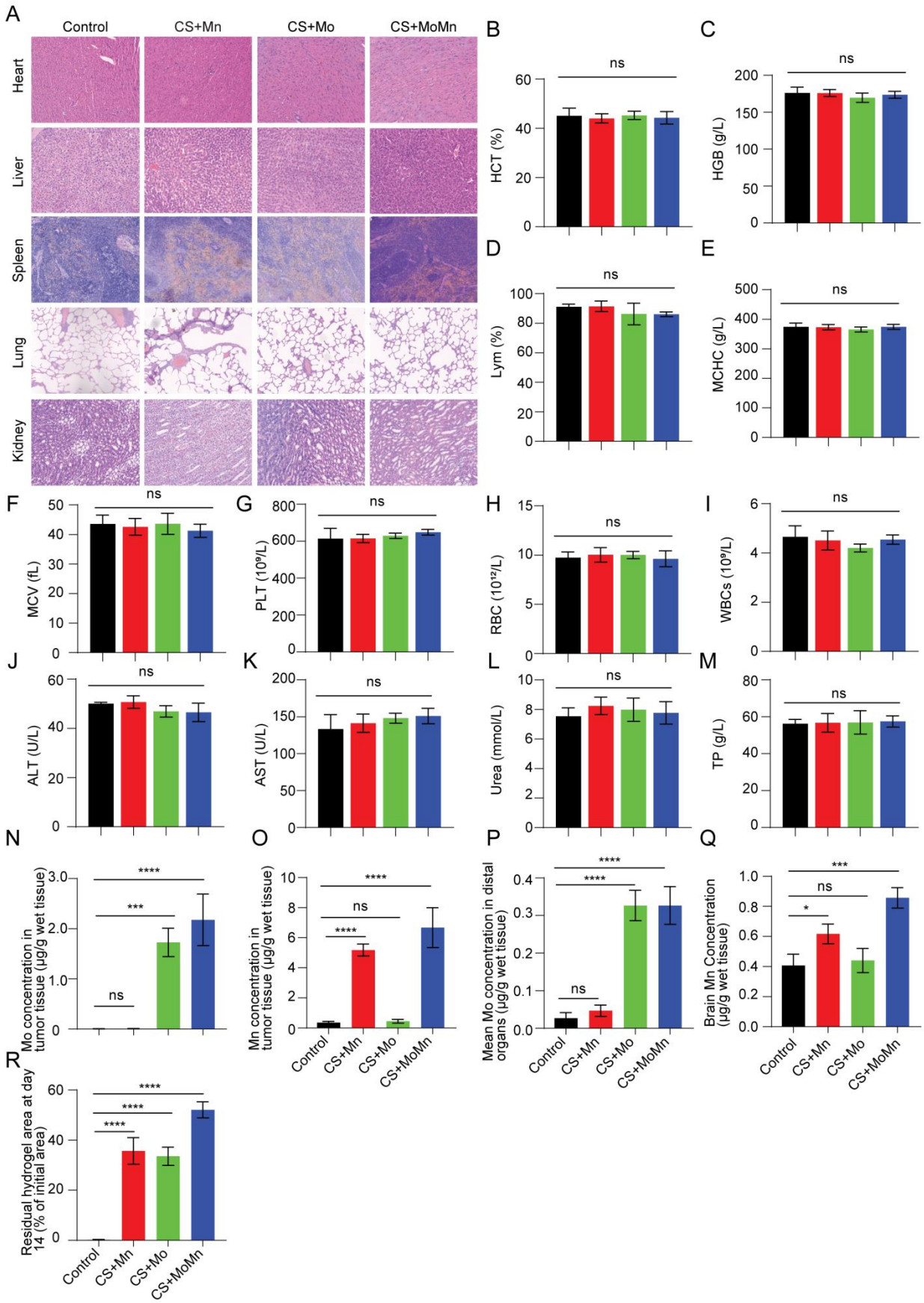

A
Control
CS+Mn
CS+Mo
CS+MoMn
Heart
Liver
Spleen
Lung
Kidney
B
HCT (%)
C
HGB (g/L)
D
Lym (%)
E
MCHC (g/L)
F
MCV (fL)
G
PLT (10⁹/L)
H
RBC (10¹²/L)
I
WBCs (10⁹/L)
J
ALT (U/L)
K
AST (U/L)
L
Urea (mmol/L)
M
TP (g/L)
N
Mo concentration in tumor tissue (μg/g wet tissue)
O
Mn concentration in tumor tissue (μg/g wet tissue)
P
Mean Mo concentration in distal organs (μg/g wet tissue)
Q
Brain Mn Concentration (μg/g wet tissue)
R
Residual hydrogel area at day 14 (% of initial area)
ns
Control
CS+Mn
CS+Mo
CS+MoMn

Figure 7. Short-term systemic tolerability, elemental biodistribution, and local hydrogel retention following intratumoral administration. (A) Representative H&E-stained sections of the heart, liver, spleen, lungs, and kidneys collected at the study endpoint. **(B–I)** Hematological parameters, including hematocrit (HCT; **B**), hemoglobin (HGB; **C**), lymphocyte percentage (Lym; **D**), mean corpuscular hemoglobin concentration (MCHC; **E**), mean corpuscular volume (MCV; **F**), platelet count (PLT; **G**), red blood cell count (RBC; **H**), and white blood cell count (WBC; **I**). **(J–M)** Serum biochemical parameters, including alanine aminotransferase (ALT; **J**), aspartate aminotransferase (AST; **K**), urea **(L)**, and total protein (TP; **M**). **(N, O)** ICP–MS quantification of Mo **(N)** and Mn **(O)** concentrations in the injected tumor tissue. **(P)** Mean Mo concentration across the analyzed distal organs. **(Q)** Mn concentration in brain tissue. **(R)** Residual hydrogel area at the injection site on day 14, expressed as a percentage of the initial hydrogel area. Data are presented as the mean ± SD (n = 4 animals per group). Each quantitative endpoint was analyzed separately using one-way ANOVA followed by Tukey's multiple-comparisons test. ns, not significant; * $p < 0.05$, *** $p < 0.001$, and **** $p < 0.0001$.

4. Discussion

The principal finding of this study is that a single 50 μL intratumoral administration of CS+MoMn markedly suppressed the growth of established subcutaneous ccRCC tumors. Compared with the unloaded hydrogel Control, CS+MoMn reduced final tumor volume by approximately 8.9 fold and decreased the calculated tumor-growth rate from 85% to 14%. This antitumor response was accompanied by reduced Ki-67 positivity, increased TUNEL positivity and tumor necrosis, decreased SLC7A11 and GPX4 abundance, and increased 4-HNE accumulation. The hydrogel also remained detectable at the injection site on day 14, while the release experiments showed that both Mo and Mn were released more rapidly under oxidative conditions than in PBS. Together, these findings support the intended function of CS+MoMn as a locally retained depot capable of oxidation-enhanced elemental release and sustained intratumoral activity.

The cellular experiments indicate that ferroptosis made a major contribution to CS+MoMn-induced ccRCC-cell death under the tested in vitro conditions. Total ROS increased following all particle-containing treatments but did not, by itself, distinguish ferroptosis from other oxidative cell-death mechanisms. In contrast, CS+MoMn produced the strongest increases in C11-BODIPY oxidation, MDA, 4-HNE, and labile Fe^{2+}, together with pronounced GSH depletion and a reduced GSH/GSSG ratio. Ferrostatin-1, liproxstatin-1, and deferoxamine substantially restored cell viability, whereas Z-VAD-FMK provided only partial protection. This rescue pattern supports iron-dependent lipid peroxidation as the major mechanism while indicating that caspase-dependent apoptosis may occur concurrently. The principal biochemical and pharmacological responses were reproduced in A498 cells, whereas HK-2 cells showed

limited cytotoxicity and no substantial increase in C11-BODIPY oxidation. This selectivity is biologically plausible because ccRCC cells enriched in oxidizable lipids depend strongly on the SLC7A11–GSH–GPX4 system to prevent lethal phospholipid peroxidation [14–16,18].

Protein and transcript analyses further supported this interpretation. CS+MoMn suppressed SLC7A11 and GPX4, increased TFRC and ACSL4, reduced FTH1, and increased 4-HNE–protein adducts. The corresponding transcriptional response included increased *PTGS2*, *CHAC1*, *ACSL4*, *TFRC*, *HMOX1*, and *NQO1*, together with reduced *SLC7A11* and *GPX4*. Although individual markers such as *PTGS2* and *CHAC1* are not independently specific for ferroptosis, their coordinated alteration with iron handling, glutathione-dependent defense, and lipid-peroxidation markers provides a coherent ferroptosis-associated molecular profile. Increased NRF2 and HO-1 likely represent an adaptive oxidative-stress response rather than an antioxidant effect of the treatment. Ferrostatin-1 and liproxstatin-1 also restored SLC7A11 and GPX4 abundance and reduced 4-HNE accumulation, providing molecular evidence consistent with the viability-rescue results. In parallel, increased caspase-3, cleaved PARP, and BAX and decreased BCL-2 supported concurrent apoptotic signaling. The dual-particle formulation consistently produced stronger effects than either single-particle formulation; however, formal synergism cannot be concluded without factorial dose–response and combination-index analyses.

The tumor-tissue findings were consistent with ferroptotic stress but do not establish that ferroptosis was required for tumor suppression in vivo. Reduced SLC7A11 and GPX4 together with increased 4-HNE demonstrate impaired lipid-peroxide defense within the treated tumors, but these markers remain associative. Establishing causality would require an in vivo rescue experiment using a ferroptosis inhibitor or tumor-cell-specific genetic manipulation of a central ferroptosis regulator. In addition, GSH depletion is not the only determinant of ferroptosis sensitivity. FSP1 and mitochondrial DHODH provide GPX4-independent antioxidant defenses [32–34], whereas cytochrome P450 oxidoreductase can promote lipid peroxidation through a separate pathway [35]. These mechanisms were not examined and may contribute to residual tumor-cell survival. Because systemic cysteine depletion can suppress tumors through disruption of a related antioxidant axis [36], and ferroptosis induction can enhance the response to radiotherapy [37], the present depot may ultimately be suitable for combination with systemic or radiation-based treatments.

The use of elemental Mo^0 also requires cautious interpretation. The weak Mo signal in the XPS survey, absence of a distinct Mo^0 diffraction peak, and lack of a Mo-specific FTIR feature are consistent with its relatively low abundance and the detection limits of these methods. These findings therefore provide limited independent structural confirmation of the Mo^0 phase within the composite. Moreover, the photothermal properties reported for MoS_2-based nanomedicines arise from the layered dichalcogenide structure and cannot be extrapolated to elemental Mo^0 [38,39]; accordingly, no photothermal mechanism is proposed here. The CS+Mo formulation also contained a lower particle mass than the CS+Mn formulation because of the selected Mo^0:α-MnO_2 ratio. Consequently, the relative effects of the single-particle groups should not be interpreted as a direct comparison of their intrinsic potencies.

The proposed therapeutic rationale instead relies on complementary redox effects. α-MnO_2 can consume the GSH antioxidant buffer [21], whereas Mo^0 was incorporated to provide a sustained local oxidative stimulus. Their combination consistently produced stronger biochemical, molecular, and antitumor responses than either component alone. At day 14, the concentrations of both Mo and Mn in the release medium were higher in 0.2 mM H_2O_2 than in PBS, supporting oxidation-enhanced elemental release under the tested conditions. Nevertheless, 0.2 mM H_2O_2 does not fully reproduce the spatially and temporally heterogeneous tumor microenvironment. Future studies should therefore examine release under more physiologically representative conditions and measure intratumoral Mo and Mn longitudinally to define their local retention, chemical speciation, and clearance.

The short-term tolerability findings were encouraging but preliminary. No overt treatment-associated lesions were observed in the major organs, and none of the evaluated hematological or serum biochemical parameters differed significantly among the groups. ICP–MS demonstrated higher Mo and Mn concentrations in the injected tumors than in the evaluated distal tissues, supporting tumor-enriched rather than exclusively tumor-confined accumulation. Residual hydrogel at the injection site further supported local depot persistence. However, detectable distal-organ Mo and increased brain Mn in the CS+MoMn group require attention. Because both manganese deficiency and excess can impair neurological function [40], longer-term biodistribution, clearance, repeated-dose, and neurobehavioral studies will be necessary before broader conclusions regarding systemic safety can be drawn.

This strategy is not intended to replace surgery for operable disease or systemic therapy for metastatic disease. Instead, it may address a defined and needle-accessible tumor mass when resection is not feasible and systemic treatments are ineffective, exhausted, or poorly tolerated [4–8]. Unlike systemic regimens that frequently require dose reduction or discontinuation because of cumulative toxicity [7,8], an intratumoral depot is designed to concentrate therapeutic activity at the tumor site while limiting the total administered dose and systemic exposure [9–11]. Nevertheless, the present evidence is limited to a single subcutaneous xenograft model with a relatively small tumor volume and short observation period. Validation in orthotopic, immunocompetent, and patient-derived models, together with optimization of injection coverage for larger tumors and longer-term safety assessment, will be required before clinical translation. Overall, the findings support CS+MoMn as a locally retained, oxidation-responsive platform that disrupts glutathione-dependent antioxidant defense, induces predominantly ferroptosis-associated ccRCC-cell death in vitro, and markedly suppresses established tumor growth in vivo.

5. Limitations

Several limitations should be acknowledged. Although the in vitro findings were reproduced in 786-O and A498 ccRCC cells and compared with HK-2 renal epithelial cells, the in vivo efficacy study used only a subcutaneous 786-O xenograft. This model does not reproduce the renal perfusion, surrounding nephron tissue, or immune microenvironment of an orthotopic tumor, and the immunodeficient host cannot resolve the potentially opposing immune consequences of ferroptotic tumor-cell death [41,42]. Validation in orthotopic, immunocompetent, and patient-derived models is therefore required. Moreover, a single 50 μL depot can cover a relatively small mouse tumor, whereas larger human lesions may require multiple image-guided injection tracks or repeated administration to overcome spatial limitations in cargo distribution [11].

All experimental groups contained the chitosan hydrogel; therefore, a composition-matched free Mo^0/α-MnO_2 control is needed to determine whether depot confinement improves retention, efficacy, and safety relative to unencapsulated particles. In addition, ferroptosis was functionally validated by pharmacological rescue only in vitro. The tumor-tissue changes in SLC7A11, GPX4, and 4-HNE remain associative, and in vivo inhibitor rescue or tumor-specific genetic manipulation would be required to establish that ferroptosis is necessary for tumor

suppression [25,43]. Finally, biodistribution was assessed at a single endpoint. Longitudinal measurements of Mo and Mn clearance, repeated-dose exposure, brain Mn accumulation, neurobehavioral outcomes, delayed toxicity, and tumor regrowth are needed to establish long-term safety and durability.

Author Contributions

Conceptualization, T.S., J.H. and P.L.; methodology, T.S., X.L. and Z.G.; validation, X.L. and Z.G.; formal analysis, T.S.; investigation, T.S. and X.L.; resources, J.H. and P.L.; data curation, T.S. and X.L.; writing—original draft preparation, T.S.; writing—review and editing, Z.G., J.H. and P.L.; visualization, T.S.; supervision, J.H. and P.L.; project administration, J.H. and P.L. All authors have read and agreed to the published version of the manuscript.

Funding

This research was funded by the General Program of the Jiangsu Provincial Geriatric Health Research Project, grant number LKM2024046; the High-Level Talent Research Start-up Fund of Huai'an First People's Hospital, grant number GQ202601; and the 2024 Research Project of the Northern Jiangsu Clinical Medicine Research Institute, grant number HAKY202400320.

Institutional Review Board Statement

The animal study protocol was reviewed and approved by the Animal Research Ethics Committee of Nanjing Medical University (Protocol code IACUC-2109025).

Consent to Participate, and Consent to Publish declarations

Not applicable.

Clinical trial number

Not applicable.

Data Availability Statement

The data presented in this study are contained within the article. Additional data are available from the corresponding authors upon reasonable request.

Conflicts of Interest

The authors declare no conflicts of interest.

References

1. Znaor, A.; Lortet-Tieulent, J.; Laversanne, M.; Jemal, A.; Bray, F. International variations and trends in renal cell carcinoma incidence and mortality. *Eur. Urol.* **2015**, *67*, 519–530.
2. Siegel, R.L.; Kratzer, T.B.; Giaquinto, A.N.; Sung, H.; Jemal, A. Cancer statistics, 2025. *CA Cancer J. Clin.* **2025**, *75*, 10–45.
3. Ljungberg, B.; Albiges, L.; Abu-Ghanem, Y.; Bedke, J.; Capitanio, U.; Dabestani, S.; Fernández-Pello, S.; Giles, R.H.; Hofmann, F.; Hora, M.; et al. European Association of Urology guidelines on renal cell carcinoma: The 2022 update. *Eur. Urol.* **2022**, *82*, 399–410.
4. Motzer, R.J.; Tannir, N.M.; McDermott, D.F.; Arén Frontera, O.; Melichar, B.; Choueiri, T.K.; Plimack, E.R.; Barthélémy, P.; Porta, C.; George, S.; et al. Nivolumab plus ipilimumab versus sunitinib in advanced renal-cell carcinoma. *N. Engl. J. Med.* **2018**, *378*, 1277–1290.
5. Rini, B.I.; Plimack, E.R.; Stus, V.; Gafanov, R.; Hawkins, R.; Nosov, D.; Pouliot, F.; Alekseev, B.; Soulières, D.; Melichar, B.; et al. Pembrolizumab plus axitinib versus sunitinib for advanced renal-cell carcinoma. *N. Engl. J. Med.* **2019**, *380*, 1116–1127.
6. Choueiri, T.K.; Powles, T.; Burotto, M.; Escudier, B.; Bourlon, M.T.; Zurawski, B.; Oyervides Juárez, V.M.; Hsieh, J.J.; Basso, U.; Shah, A.Y.; et al. Nivolumab plus cabozantinib versus sunitinib for advanced renal-cell carcinoma. *N. Engl. J. Med.* **2021**, *384*, 829–841.
7. Motzer, R.J.; Hutson, T.E.; Tomczak, P.; Michaelson, M.D.; Bukowski, R.M.; Rixe, O.; Oudard, S.; Negrier, S.; Szczylik, C.; Kim, S.T.; et al. Sunitinib versus interferon alfa in metastatic renal-cell carcinoma. *N. Engl. J. Med.* **2007**, *356*, 115–124.
8. Brown, J.E.; Royle, K.L.; Gregory, W.; Ralph, C.; Maraveyas, A.; Din, O.; Eisen, T.; Nathan, P.; Powles, T.; Griffiths, R.; et al. Temporary treatment cessation versus continuation of first-line tyrosine kinase inhibitor in patients with advanced clear cell renal cell carcinoma (STAR): An open-label, non-inferiority, randomised, controlled, phase 2/3 trial. *Lancet Oncol.* **2023**, *24*, 213–227.
9. Marabelle, A.; Tselikas, L.; de Baere, T.; Houot, R. Intratumoral immunotherapy: Using the tumor as the remedy. *Ann. Oncol.* **2017**, *28*, xii33–xii43.

10. Melero, I.; Castanon, E.; Alvarez, M.; Champiat, S.; Marabelle, A. Intratumoural administration and tumour-tissue targeting of cancer immunotherapies. *Nat. Rev. Clin. Oncol.* **2021**, *18*, 558–576.
11. Minchinton, A.I.; Tannock, I.F. Drug penetration in solid tumours. *Nat. Rev. Cancer* **2006**, *6*, 583–592.
12. Chenite, A.; Chaput, C.; Wang, D.; Combes, C.; Buschmann, M.D.; Hoemann, C.D.; Leroux, J.C.; Atkinson, B.L.; Binette, F.; Selmani, A. Novel injectable neutral solutions of chitosan form biodegradable gels *in situ*. *Biomaterials* **2000**, *21*, 2155–2161.
13. Mikhail, A.S.; Morhard, R.; Mauda-Havakuk, M.; Kassin, M.; Arrichiello, A.; Wood, B.J. Hydrogel drug-delivery systems for minimally invasive local immunotherapy of cancer. *Adv. Drug Deliv. Rev.* **2023**, *202*, 115083.
14. Zou, Y.; Palte, M.J.; Deik, A.A.; Li, H.; Eaton, J.K.; Wang, W.; Tseng, Y.Y.; Deasy, R.; Kost-Alimova, M.; Dančík, V.; et al. A GPX4-dependent cancer-cell state underlies the clear-cell morphology and confers sensitivity to ferroptosis. *Nat. Commun.* **2019**, *10*, 1617.
15. Yang, W.S.; SriRamaratnam, R.; Welsch, M.E.; Shimada, K.; Skouta, R.; Viswanathan, V.S.; Cheah, J.H.; Clemons, P.A.; Shamji, A.F.; Clish, C.B.; et al. Regulation of ferroptotic cancer-cell death by GPX4. *Cell* **2014**, *156*, 317–331.
16. Friedmann Angeli, J.P.; Schneider, M.; Proneth, B.; Tyurina, Y.Y.; Tyurin, V.A.; Hammond, V.J.; Herbach, N.; Aichler, M.; Walch, A.; Eggenhofer, E.; et al. Inactivation of the ferroptosis regulator GPX4 triggers acute renal failure in mice. *Nat. Cell Biol.* **2014**, *16*, 1180–1191.
17. Ingold, I.; Berndt, C.; Schmitt, S.; Doll, S.; Poschmann, G.; Buday, K.; Roveri, A.; Peng, X.; Porto Freitas, F.; Seibt, T.; et al. Selenium utilization by GPX4 is required to prevent hydroperoxide-induced ferroptosis. *Cell* **2018**, *172*, 409–422.e21.
18. Koppula, P.; Zhuang, L.; Gan, B. Cystine transporter SLC7A11/xCT in cancer: Ferroptosis, nutrient dependency, and cancer therapy. *Protein Cell* **2021**, *12*, 599–620.
19. Dixon, S.J.; Lemberg, K.M.; Lamprecht, M.R.; Skouta, R.; Zaitsev, E.M.; Gleason, C.E.; Patel, D.N.; Bauer, A.J.; Cantley, A.M.; Yang, W.S.; et al. Ferroptosis: An iron-dependent form of nonapoptotic cell death. *Cell* **2012**, *149*, 1060–1072.
20. Jiang, X.; Stockwell, B.R.; Conrad, M. Ferroptosis: Mechanisms, biology and role in disease. *Nat. Rev. Mol. Cell Biol.* **2021**, *22*, 266–282.

21. Lin, L.S.; Song, J.; Song, L.; Ke, K.; Liu, Y.; Zhou, Z.; Shen, Z.; Li, J.; Yang, Z.; Tang, W.; et al. Simultaneous Fenton-like ion delivery and glutathione depletion by MnO_2-based nanoagent to enhance chemodynamic therapy. *Angew. Chem. Int. Ed.* **2018**, *57*, 4902–4906.
22. Prasad, P.; Gordijo, C.R.; Abbasi, A.Z.; Maeda, A.; Ip, A.; Rauth, A.M.; DaCosta, R.S.; Wu, X.Y. Multifunctional albumin–MnO_2 nanoparticles modulate the solid-tumor microenvironment by attenuating hypoxia, acidosis, and vascular endothelial growth factor and enhance the radiation response. *ACS Nano* **2014**, *8*, 3202–3212.
23. Abbasi, A.Z.; Gordijo, C.R.; Amini, M.A.; Maeda, A.; Rauth, A.M.; DaCosta, R.S.; Wu, X.Y. Hybrid manganese dioxide nanoparticles potentiate radiation therapy by modulating tumor hypoxia. *Cancer Res.* **2016**, *76*, 6643–6656.
24. Yang, G.; Xu, L.; Chao, Y.; Xu, J.; Sun, X.; Wu, Y.; Peng, R.; Liu, Z. Hollow MnO_2 as a tumor-microenvironment-responsive biodegradable nanoplatform for combination therapy favoring antitumor immune responses. *Nat. Commun.* **2017**, *8*, 902.
25. Nghiem, T.-H.T.; Kusuma, F.; Park, J.; Joe, Y.; Chung, H.T.; Han, J. Brief guide to detecting ferroptosis. *Mol. Cells* **2025**, *48*, 100276.
26. Doll, S.; Proneth, B.; Tyurina, Y.Y.; Panzilius, E.; Kobayashi, S.; Ingold, I.; Irmler, M.; Beckers, J.; Aichler, M.; Walch, A.; et al. ACSL4 dictates ferroptosis sensitivity by shaping cellular lipid composition. *Nat. Chem. Biol.* **2017**, *13*, 91–98.
27. Kagan, V.E.; Mao, G.; Qu, F.; Friedmann Angeli, J.P.; Doll, S.; Croix, C.S.; Dar, H.H.; Liu, B.; Tyurin, V.A.; Ritov, V.B.; et al. Oxidized arachidonic and adrenic phosphatidylethanolamines navigate cells to ferroptosis. *Nat. Chem. Biol.* **2017**, *13*, 81–90.
28. Yang, W.S.; Kim, K.J.; Gaschler, M.M.; Patel, M.; Shchepinov, M.S.; Stockwell, B.R. Peroxidation of polyunsaturated fatty acids by lipoxygenases drives ferroptosis. *Proc. Natl. Acad. Sci. USA* **2016**, *113*, E4966–E4975.
29. Bustin, S.A.; Ruijter, J.M.; van den Hoff, M.J.B.; Kubista, M.; Pfaffl, M.W.; Shipley, G.L.; Tran, N.; Rödiger, S.; Untergasser, A.; Mueller, R.; et al. MIQE 2.0: Revision of the minimum information for publication of quantitative real-time PCR experiments guidelines. *Clin. Chem.* **2025**, *71*, 634–651.
30. Percie du Sert, N.; Hurst, V.; Ahluwalia, A.; Alam, S.; Avey, M.T.; Baker, M.; Browne, W.J.; Clark, A.; Cuthill, I.C.; Dirnagl, U.; et al. The ARRIVE guidelines 2.0: Updated guidelines for reporting animal research. *PLoS Biol.* **2020**, *18*, e3000410.

31. Conrad, M.; Friedmann Angeli, J.P.; Vandenabeele, P.; Stockwell, B.R. Regulated necrosis: Disease relevance and therapeutic opportunities. *Nat. Rev. Drug Discov.* **2016**, *15*, 348–366.
32. Doll, S.; Freitas, F.P.; Shah, R.; Aldrovandi, M.; da Silva, M.C.; Ingold, I.; Goya Grocin, A.; Xavier da Silva, T.N.; Panzilius, E.; Scheel, C.H.; et al. FSP1 is a glutathione-independent ferroptosis suppressor. *Nature* **2019**, *575*, 693–698.
33. Bersuker, K.; Hendricks, J.M.; Li, Z.; Magtanong, L.; Ford, B.; Tang, P.H.; Roberts, M.A.; Tong, B.; Maimone, T.J.; Zoncu, R.; et al. The CoQ oxidoreductase FSP1 acts parallel to GPX4 to inhibit ferroptosis. *Nature* **2019**, *575*, 688–692.
34. Mao, C.; Liu, X.; Zhang, Y.; Lei, G.; Yan, Y.; Lee, H.; Koppula, P.; Wu, S.; Zhuang, L.; Fang, B.; et al. DHODH-mediated ferroptosis defence is a targetable vulnerability in cancer. *Nature* **2021**, *593*, 586–590.
35. Koppula, P.; Zhuang, L.; Gan, B. POR is a ferroptosis fuel. *Protein Cell* **2021**, *12*, 675–679.
36. Badgley, M.A.; Kremer, D.M.; Maurer, H.C.; DelGiorno, K.E.; Lee, H.J.; Purohit, V.; Sagalovskiy, I.R.; Ma, A.; Kapilian, J.; Firl, C.E.M.; et al. Cysteine depletion induces pancreatic tumor ferroptosis in mice. *Science* **2020**, *368*, 85–89.
37. Lei, G.; Mao, C.; Yan, Y.; Zhuang, L.; Gan, B. Ferroptosis, radiotherapy, and combination therapeutic strategies. *Protein Cell* **2021**, *12*, 836–857.
38. Feng, W.; Chen, L.; Qin, M.; Zhou, X.; Zhang, Q.; Miao, Y.; Qiu, K.; Zhang, Y.; He, C. Flower-like PEGylated MoS_2 nanoflakes for near-infrared photothermal cancer therapy. *Sci. Rep.* **2015**, *5*, 17422.
39. Liu, T.; Wang, C.; Cui, W.; Gong, H.; Liang, C.; Shi, X.; Li, Z.; Sun, B.; Liu, Z. Combined photothermal and photodynamic therapy delivered by PEGylated MoS_2 nanosheets. *Nanoscale* **2014**, *6*, 11219–11225.
40. Balachandran, R.C.; Mukhopadhyay, S.; McBride, D.; Veevers, J.; Harrison, F.E.; Aschner, M.; Haynes, E.N.; Bowman, A.B. Brain manganese and the balance between essential roles and neurotoxicity. *J. Biol. Chem.* **2020**, *295*, 6312–6329.
41. Efimova, I.; Catanzaro, E.; Van der Meeren, L.; Turubanova, V.D.; Hammad, H.; Mishchenko, T.A.; Vedunova, M.V.; Fimognari, C.; Bachert, C.; Coppieters, F.; et al. Vaccination with early ferroptotic cancer cells induces efficient antitumor immunity. *J. Immunother. Cancer* **2020**, *8*, e001369.

42. Wiernicki, B.; Maschalidi, S.; Pinney, J.; Adjemian, S.; Vanden Berghe, T.; Ravichandran, K.S.; Vandenabeele, P. Cancer cells dying from ferroptosis impede dendritic-cell-mediated antitumor immunity. *Nat. Commun.* **2022**, *13*, 3676.

43. Zilka, O.; Shah, R.; Li, B.; Friedmann Angeli, J.P.; Griesser, M.; Conrad, M.; Pratt, D.A. On the mechanism of cytoprotection by ferrostatin-1 and liproxstatin-1 and the role of lipid peroxidation in ferroptotic cell death. *ACS Cent. Sci.* **2017**, *3*, 232–243.